

AFRL-RW-EG-TR-2009-7017

## Development of a Multi-Scale Methodology for Prediction of the Macroscopic Anisotropic Stress-Strain Response of Textured Metals under Dynamic Loading

---

Oana Cazacu

Department of Mechanical and Aerospace Engineering  
University of Florida, REEF  
1350 N Poquito Rd  
Shalimar, FL 32579



CONTRACT NO. FA8651-05-1-0005

January 21, 2009

FINAL REPORT FOR PERIOD June 2005 - January 2009

DISTRIBUTION A: Approved for public release; distribution unlimited. 96<sup>th</sup> ABW/PA Approval and Clearance # 96ABW-2009-0045, dated 9 Feb 2009

**AIR FORCE RESEARCH LABORATORY, MUNITIONS DIRECTORATE**

■ Air Force Materiel Command    ■ United States Air Force    ■ Eglin Air Force Base

## NOTICE AND SIGNATURE PAGE

Using Government drawings, specifications, or other data included in this document for any purpose other than Government procurement does not in any way obligate the U.S. Government. The fact that the Government formulated or supplied the drawings, specifications, or other data does not license the holder or any other person or corporation; or convey any rights or permission to manufacture, use, or sell any patented invention that may relate to them.

This report was cleared for public release by the 96 Air Base Wing, Public Affairs Office, and is available to the general public, including foreign nationals. Copies may be obtained from the Defense Technical Information Center (DTIC) <<http://www.dtic.mil/dtic/index.html>>.

AFRL-RW-EG-TR-2009-7017 HAS BEEN REVIEWED AND IS APPROVED FOR PUBLICATION IN ACCORDANCE WITH ASSIGNED DISTRIBUTION STATEMENT.

FOR THE DIRECTOR:

\_\_\_\_\_/SIGNED/\_\_\_\_\_  
Azar S. Ali  
Technical Director  
Assessment and Demonstrations Division

\_\_\_\_\_/SIGNED/\_\_\_\_\_  
Martin J. Schmidt  
Mechanical Engineer  
Computational Mechanics Branch

This report is published in the interest of scientific and technical information exchange, and its publication does not constitute the Government's approval or disapproval of its ideas or findings.

# REPORT DOCUMENTATION PAGE

*Form Approved*  
OMB No. 0704-0188

Public reporting burden for this collection of information is estimated to average 1 hour per response, including the time for reviewing instructions, searching existing data sources, gathering and maintaining the data needed, and completing and reviewing this collection of information. Send comments regarding this burden estimate or any other aspect of this collection of information, including suggestions for reducing this burden to Department of Defense, Washington Headquarters Services, Directorate for Information Operations and Reports (0704-0188), 1215 Jefferson Davis Highway, Suite 1204, Arlington, VA 22202-4302. Respondents should be aware that notwithstanding any other provision of law, no person shall be subject to any penalty for failing to comply with a collection of information if it does not display a currently valid OMB control number. **PLEASE DO NOT RETURN YOUR FORM TO THE ABOVE ADDRESS.**

<b>1. REPORT DATE (DD-MM-YYYY)</b> 21-01-2009		<b>2. REPORT TYPE</b> FINAL		<b>3. DATES COVERED (From - To)</b> June 2005 - January 2009	
<b>4. TITLE AND SUBTITLE</b>  Development of a Multi-Scale Methodology for Prediction of the Macroscopic Anisotropic Stress-Strain Response of Textured Metals under Dynamic Loading				<b>5a. CONTRACT NUMBER</b>	
				<b>5b. GRANT NUMBER</b> FA 8651-05-1-0005	
				<b>5c. PROGRAM ELEMENT NUMBER</b> 62602F	
<b>6. AUTHOR(S)</b> Oana Cazacu				<b>5d. PROJECT NUMBER</b> 2502	
				<b>5e. TASK NUMBER</b> 07	
				<b>5f. WORK UNIT NUMBER</b> 39	
<b>7. PERFORMING ORGANIZATION NAME(S) AND ADDRESS(ES)</b>  Department of Mechanical and Aerospace Engineering, University of Florida, REEF 1350 N Poquito Rd Shalimar, FL 32579				<b>8. PERFORMING ORGANIZATION REPORT NUMBER</b>	
<b>9. SPONSORING / MONITORING AGENCY NAME(S) AND ADDRESS(ES)</b> Air Force Research Laboratory, Munitions Directorate AFRL/RWAC 101 West Eglin Boulevard Eglin AFB, FL 32542-6810				<b>10. SPONSOR/MONITOR'S ACRONYM(S)</b> AFRL-RW-EG	
				<b>11. SPONSOR/MONITOR'S REPORT NUMBER(S)</b> AFRL-RW-EG-TR-2009-7017	
<b>12. DISTRIBUTION / AVAILABILITY STATEMENT</b> <b>DISTRIBUTION A: Approved for public release; distribution unlimited. 96<sup>th</sup> ABW/PA Approval and Clearance #96ABW-2009-0045 , dated 9 Feb 2009</b>					
<b>13. SUPPLEMENTARY NOTES</b>					
<b>14. ABSTRACT</b> This report documents a comprehensive experimental and theoretical investigation of the deformation behavior of high-purity, polycrystalline alpha-titanium. A series of monotonic uniaxial compression and tension tests were carried out at room temperature under quasi-static conditions to quantify the plastic anisotropy and the tension-compression asymmetry of this material. The evolution of microstructure and texture during deformation was studied using optical image microscopy (OIM) and neutron-diffraction techniques to elucidate the role of deformation twinning and its effect on the macroscopic response. To characterize the material's strain rate sensitivity, Split Hopkinson Pressure Bar tests at strain rates of 400 to 600 sec <sup>-1</sup> were performed along the axes of symmetry of the material. The experimental activities were complemented with multi-scale model development in the framework of plasticity theory. To describe the quasi-static macroscopic response of the material, a new anisotropic elastic/plastic model was developed. Key in its formulation is a yield criterion that captures strength differential effects. Anisotropy was introduced through a linear transformation on the Cauchy stress tensor applied to the material. This integrated experimental-theoretical effort appears to have resulted in the description, for the first time, of the anisotropic stress-response of high-purity titanium at room temperature.					
<b>15. SUBJECT TERMS</b> Plasticity, tension-compression asymmetry, anisotropic, titanium					
<b>16. SECURITY CLASSIFICATION OF:</b>			<b>17. LIMITATION OF ABSTRACT</b>	<b>18. NUMBER OF PAGES</b>	<b>19a. NAME OF RESPONSIBLE PERSON</b> Martin J Schmidt
<b>a. REPORT</b> UNCLASSIFIED	<b>b. ABSTRACT</b> UNCLASSIFIED	<b>c. THIS PAGE</b> UNCLASSIFIED			<b>19b. TELEPHONE NUMBER (include area code)</b>

This material is based on research sponsored by the Air Force Research Laboratory Munitions Directorate, under agreement number **FA 8651-05-1-0005**. The U.S. Government is authorized to reproduce and distribute reprints for Governmental purposes notwithstanding any copyright notation thereon.

The views and conclusions contained herein are those of the author and should not be interpreted as necessarily representing the official policies or endorsements, either expressed or implied, of the Air Force Research Laboratory or the U.S. Government.

## Abstract

This report documents a comprehensive experimental and theoretical investigation of the deformation behavior of high-purity, polycrystalline  $\alpha$ -titanium. A series of monotonic uniaxial compression and tension tests were carried out at room temperature under quasi-static conditions to quantify the plastic anisotropy and the tension-compression asymmetry of this material. The evolution of microstructure and texture during deformation was studied using optical image microscopy (OIM) and neutron-diffraction techniques to elucidate the role of deformation twinning and its effect on the macroscopic response. In addition, four-point bending tests were conducted. As a result of the anisotropy and directionality of twinning, qualitative differences between the response of upper and lower fibers in different orientations were observed. To characterize the material's strain rate sensitivity, Split Hopkinson Pressure Bar tests at strain rates of 400 to 600  $\text{sec}^{-1}$  were performed along the axes of symmetry of the material. A clear increase in strength with increasing strain rate is observed, the hardening rate remaining practically unchanged for all directions, with the exception of the rolling direction. The dramatic hardening rate increase in the rolling direction was indicative of higher propensity for twinning with increasing strain rate. Based on the experimental data, it can be concluded that the material has a very complex anisotropic behavior and exhibits tension/compression asymmetry and strain rate sensitivity.

The experimental activities were complemented with multi-scale model development in the framework of plasticity theory. To describe the quasi-static macroscopic response of the material, a new anisotropic elastic/plastic model was developed. Key in its formulation is a yield criterion that captures strength differential effects. Anisotropy was introduced through a linear transformation on the Cauchy stress tensor applied to the material. An anisotropic hardening rule that accounts for texture evolution associated to twinning was developed. It was demonstrated that the proposed model describes very well the main features of the quasi-static response of high-purity titanium when subjected to monotonic loading conditions. Validation of the model was provided through comparison between measured and simulated strain distributions in bending. In particular, the shift of the neutral axis was well described. Rate effects on the behavior of the material were also investigated. This integrated experimental-theoretical effort appears to have resulted in the description, for the first time, of the anisotropic stress-response of high-purity  $\alpha$ -titanium at room temperature.

# Contents

<b>1</b>	<b>Introduction</b>	<b>4</b>
<b>2</b>	<b>Experimental procedures</b>	<b>7</b>
2.1	Material . . . . .	7
2.2	Quasi-static behavior of high-purity $\alpha$ -titanium . . . . .	8
2.2.1	Microstructure evolution during uniaxial compression deformation . . . . .	11
2.2.2	Four-Point Beam Bending Test Results . . . . .	21
<b>3</b>	<b>Proposed model for description of the elastic-plastic deformation of high-purity <math>\alpha</math>-titanium</b>	<b>26</b>
3.1	Proposed yield criterion . . . . .	26
3.1.1	Isotropic yield function . . . . .	26
3.2	Proposed orthotropic criterion . . . . .	27
3.3	Modeling anisotropic hardening during monotonic deformation of $\alpha$ -titanium . . . . .	32
3.4	Integration algorithm of the proposed model, finite-element implementation, and simulation of the response of high-purity $\alpha$ titanium in uniaxial tension/compression . . . . .	34
3.5	Application of the proposed model to $\alpha$ -titanium . . . . .	37
3.6	Model validation results . . . . .	40
<b>4</b>	<b>Characterization of the high-strain rate behavior of high-purity <math>\alpha</math>-titanium</b>	<b>54</b>
<b>5</b>	<b>Discussion and Conclusions</b>	<b>60</b>
<b>6</b>	<b>References</b>	<b>61</b>

# 1 Introduction

Because of their outstanding engineering properties such as corrosion resistance, 200,000  $lb/in^2$  strength, moderate weight (40% lighter than steel) and high strengths, good formability, and biocompatibility, titanium and its alloys have found widespread use in high-performance applications. For example, titanium and its alloys are widely used for aircraft structures requiring greater heat resistance than aluminum alloys because of their high strength-to-weight ratio. Also, titanium alloys are leading candidates for metal-matrix composites, primarily for aircraft engine applications. The stress-strain response of titanium at high strain-rates and its alloys is receiving continued attention, which is related to platform calculations for crash-worthiness and foreign-object damage in aerospace systems, ballistic and armor applications, high-rate forming, and high-rate machining [1]. The defense industry is also interested in advancing the application of titanium alloys to armor systems.

Pure titanium has a hexagonal close-packed (HCP) structure with  $c/a$  ratio of 1.587 lower than the ideal  $c/a$  ratio of 1.633. There are three principal types of titanium alloys:  $\alpha$  or near- $\alpha$  alloys,  $\alpha - \beta$  alloys, and  $\beta$  alloys. Titanium alloys in the low and medium temperature regime mainly consist of the HCP  $\alpha$ -phase with very little dispersed  $\beta$  phase in between the  $\alpha$  grains. Considerable efforts have been devoted to the characterization and modeling the response of titanium alloys (see for example, [2], [3], [4], [5], [6], [7], etc.). The experimental data reported concerned mainly the uniaxial and torsional responses at different strain rates and temperatures while data for non-proportional loading paths is rather limited (see [7]). Many studies have also been devoted to the understanding of the specific plastic deformation mechanisms at room temperature in pure titanium (e.g. see [1]; [8] for data on high-purity  $\alpha$  titanium; [9] and [10] for commercial purity titanium). Two types of deformation modes, slip and twinning, occur in titanium and its alloys during plastic deformation at room temperature. It is generally agreed that pronounced yield asymmetry is associated with the activation of twinning. Previous studies ([7], [11], [13], etc.) have also shown that classic plasticity models, such as  $J_2$  plasticity, or Hill [12] are unable to capture this asymmetry that results from the combination of a sharp initial basal texture and the polarity of deformation twinning. Twinning plays two important roles in  $\alpha$  titanium. It is a main contributor to texture evolution by reorienting the twinned areas (see [10]) even for the simplest monotonic loading paths. Furthermore, twinning drastically influences the strain hardening behavior (see for example [8]). Accurate and realistic modeling of the behavior of  $\alpha$  titanium thus requires incorporation of the effects of twinning on the mechanical response. Since in crystal plasticity models the distribution of crystal orientations in the given polycrystal, the available slip/twinning deformation systems and the stress levels necessary to activate them are taken into account explicitly, the evolution of anisotropy due to texture development can be characterized by measuring the initial texture and updating the texture using a suitable homogenization scheme such as Taylor or self-consistent model (see [14]). Recently, the application of crystal plasticity models to hexagonal metals and the incorporation of crystal plasticity calculations directly into finite element (FE) analyzes have received much attention. Models that account for both slip and twinning activity and employ Taylor (e.g.[15], [16] or self-consistent ([17], [18], etc.) averaging schemes to predict the aggregate behavior

have been proposed. For example, [16] concentrated their attention on the development of slip-hardening and twin-hardening functions based on the experimental data on high purity titanium deformed in simple compression reported in [8]. These laws were incorporated into a Taylor crystal plasticity framework and further used to simulate the stress-strain response and texture evolution for monotonic loading (uniaxial compression and simple shear). However, no attempt was made to predict the final deformed shape of the specimens, nor to perform benchmark simulations of more complex monotonic loadings such as bending. In [19] a self-consistent viscoplastic model linked to the explicit FE code EPIC has been successfully used for describing the deformation of pure zirconium with a strong initial texture under quasi-static monotonic loading at room and liquid nitrogen temperatures. The above direct implementations of polycrystal models into FE codes, where a polycrystalline aggregate is associated with each FE integration point, have the advantage that they follow the evolution of anisotropy due to texture development. However, such FE calculations are computationally very intensive, thus limiting the applicability of these approaches to problems that do not require a fine spatial resolution.

An alternative promising approach is to develop anisotropic formulations at a macroscopic level that can be easily implemented in FE codes, and thus can be applied routinely for detailed analyzes of complex forming processes. Unlike recent progress in the development of mathematical descriptions of anisotropic yield surfaces for materials with cubic structure (for a review of such formulations see [20], [21] [22], etc.), macroscopic level modeling of yielding and strain-hardening of HCP materials is less developed. Some of the rigorous methods proposed to account for initial plastic anisotropy or to describe an average material response over a certain deformation range (see [23]) can be extended to HCP materials. The major difficulty encountered in formulating analytic expressions for the yield functions of hcp metals is related to the description of the tension-compression asymmetry associated to twinning. Recently, yield functions in the three-dimensional stress space that describe both the tension-compression asymmetry and the anisotropic behavior of HCP metals have been developed. To describe yielding asymmetry that results either from twinning or from non-Schmidt effects at single crystal level, Cazacu and Barlat [24] have proposed an isotropic criterion expressed in terms of all invariants of the stress deviator. This isotropic yield criterion was applied to the description of crystal plasticity simulation results of [25] and that of [26] for randomly oriented polycrystals (for more details, see [27]). This isotropic criterion was further extended such as to incorporate anisotropy using the generalized invariants approach proposed by [21]. Comparison between this orthotropic criterion and data on magnesium and its alloys by [30] and titanium (data after [11]) show that this anisotropic model accurately describes both anisotropy and tension-compression asymmetry in yielding of these materials. In [29] another isotropic pressure-insensitive yield criterion that accounts for yielding asymmetry between tension and compression associated with deformation twinning was developed. This isotropic criterion involves all principal values of the stress deviator. To account for both strength differential effects and texture-induced anisotropy, an extension of this criterion using one linear transformation operator  $\mathbf{L}$  operating on the Cauchy stress deviator was proposed by [29]. The orthotropic yield criterion [29] was shown to exhibit accuracy in describing the yield loci of magnesium (see [28],

[29]) and titanium alloys ([29], [6] and [7]). A macroscopic model that captures the evolution of anisotropy due to evolving texture in hexagonal metals subjected to monotonic loading conditions was proposed by [31]. Yielding was described using the orthotropic yield criterion [29]. To model the change in shape of the yield locus due to twinning reorientation of the lattice, evolution laws for the anisotropic coefficients involved in the expression of the yield criterion [29] were developed using a multi-scale procedure based on crystal plasticity calculations of flow stresses with the self-consistent viscoplastic model (VPSC) model [32] and macroscopic scale interpolation techniques. Experimental crystallographic textures and stress-strain curves were used as input. This approach was successfully applied to the description of the behavior of zirconium at room temperature when subjected to quasi-static deformation ([31]) or dynamic loading ([33], [34])

This study presents a comprehensive set of experiments aimed at understanding the response of high-purity titanium at room temperature and consequently modeling the observed response at different strain rates. A series of monotonic quasi-static uniaxial tension and compression tests were conducted to quantify the plastic anisotropy and the tension-compression asymmetry of this material. In addition, four-point bending tests were carried out. To characterize the material's strain rate sensitivity, Split Hopkinson Pressure Bar tests at strain rates of 400 to 600  $\text{sec}^{-1}$  were performed along the axes of symmetry of the material. To gain insight into the deformation mechanisms, OIM and texture evaluations were also conducted in conjunction with the mechanical tests. The experimental activities were complemented with multi-scale model development in the framework of plasticity. The material parameter identification procedure will be outlined. The algorithmic aspects related to the implementation of the models developed in the FE code EPIC will be presented in detail. The ability of the proposed model to capture the main features of the observed behavior will be examined by comparing the experimental data with simulation results in terms of stress-strain response in tension/compression and bending for different orientations with respect to the axes of symmetry of the material.

We shall use the following notations. The inner product of two vectors  $\mathbf{v}$  and  $\mathbf{u}$  will be denoted by  $\mathbf{v} \cdot \mathbf{u}$ . The dyadic product of two vectors  $\mathbf{v}$  and  $\mathbf{u}$  will be denoted by  $\mathbf{v} \otimes \mathbf{u}$ . Superscript  $T$  indicates the transpose operation  $(\mathbf{A}^T)_{ij} = A_{ji}$  for any second-order tensor  $\mathbf{A}$  while symbol 'tr' denotes the trace operator applied to second-order tensors, i.e.  $\text{tr}(\mathbf{A}) = A_{ii}$ . The symmetric part of any second-order tensor  $\mathbf{A}$  is denoted by  $\mathbf{A}^{symm}$  and is defined as  $\mathbf{A}^{symm} = \frac{1}{2}(\mathbf{A} + \mathbf{A}^T)$ ; the antisymmetric part of any second-order tensor  $\mathbf{A}$  is denoted by  $\mathbf{A}^{skew}$  and is defined as  $\mathbf{A}^{skew} = \frac{1}{2}(\mathbf{A} - \mathbf{A}^T)$ . The second-order identity tensor is denoted by  $\mathbf{I}$ . The inner product of two second-order tensors  $\mathbf{A}$  and  $\mathbf{B}$  is defined by  $\mathbf{A} \cdot \mathbf{B} = \text{tr}(\mathbf{A}^T \mathbf{B})$ , the product between a fourth-order tensor  $\mathbf{P}$  and a second-order tensor  $\mathbf{C}$  is the second-order tensor defined as  $(\mathbf{C} : \mathbf{P})_{ij} = C_{ijkl} P_{kl}$ .

## 2 Experimental procedures

High-purity  $\alpha$ -titanium was mechanically tested at room temperature under both quasi-static and high loading rates. To gain insight into the deformation mechanisms, texture measurements were carried out in conjunction with the mechanical tests at Los Alamos National Laboratory (LANL). Both OIM and neutron diffraction techniques were used to evaluate texture evolution along each loading path.

### 2.1 Material

The material used in this work was high purity (99.999%) titanium that was purchased from Alpha Aesar of Johnson Matthey Electronics, Inc., (Spokane, WA). The material was supplied in the form of a 15.87 mm thick cross-rolled disk of 254 mm diameter. Optical microscopy showed that the as received material has equiaxed grains with an average grain size of about 20  $\mu\text{m}$  (Fig. 1).

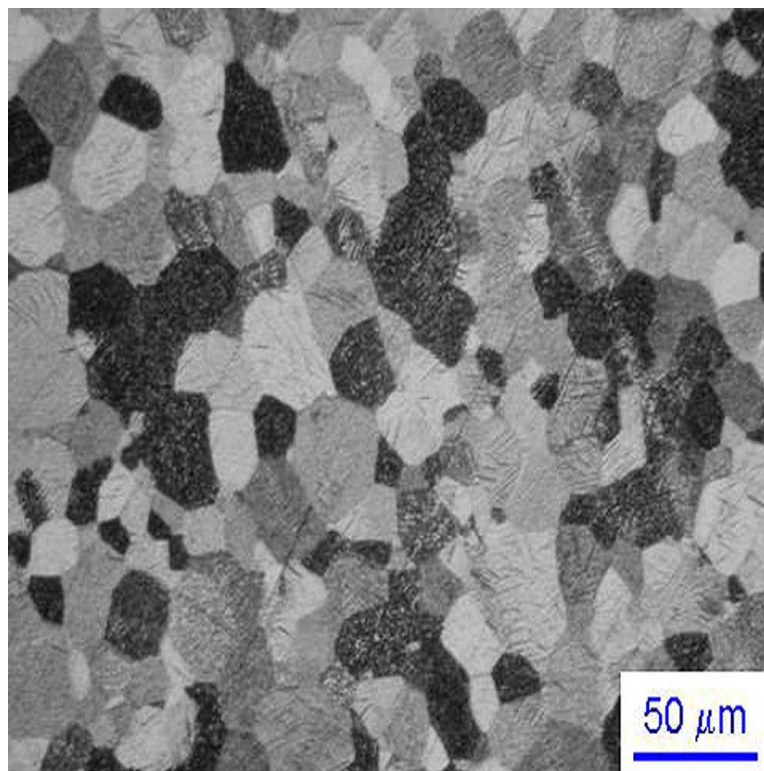


Figure 1: Micrograph of the high-purity titanium plate material

Twenty samples were removed using water jet from the perimeter of the plate. Each sample is approximately 19.05 mm x 19.05 mm x 19.05 mm and 11.32° from the neighboring sample (see Fig. 2). The basal plane (0002) figures were analyzed to determine the rolling direction (RD),

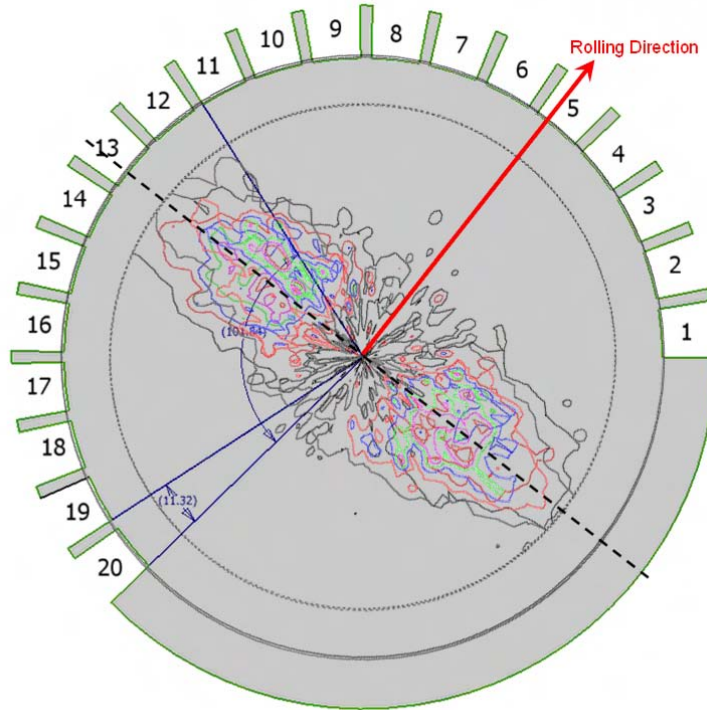


Figure 2: Measured pole figure of the basal plane (0002); the rolling direction (RD) is indicated in red.

which was subsequently marked on the plate as shown in Figure 2. Note that the plate exhibits fiber texture resulting from the rolling process. The basal plane aligns at  $30^\circ$  to  $40^\circ$  from the plate normal. This result was also confirmed by the analysis of the [0001] pole figures obtained from neutron diffraction measurements of the initial texture (see Figure 3) carried out on the neutron time-of-flight (TOF) diffractometer HIPPO (High-Pressure-Preferred Orientation) at LANSCE (Los Alamos Neutron Science Center).

## 2.2 Quasi-static behavior of high-purity $\alpha$ -titanium

The quasi-static characterization tests consisted of uniaxial tension and compression tests that were conducted at room temperature and at a nominal strain rate of  $0.001 \text{ sec}^{-1}$ , using an Instron 1125 testing machine. Test specimens were cut from the plate using Electrical Discharge Machining (EDM) in order to eliminate artificial hardening that may occur using other machining techniques. Tensile testing was carried out with a 5 KN load cell and an Instron model number G-51-12-A extensometer with a gauge length of 25.4 mm. To characterize the anisotropy of the material, standard tensile specimens were machined such the tensile direction was either parallel to the rolling direction (RD), transverse direction (TD), or  $45^\circ$  to the rolling direction, respectively (see Figure 4 for the dimensions of the samples).

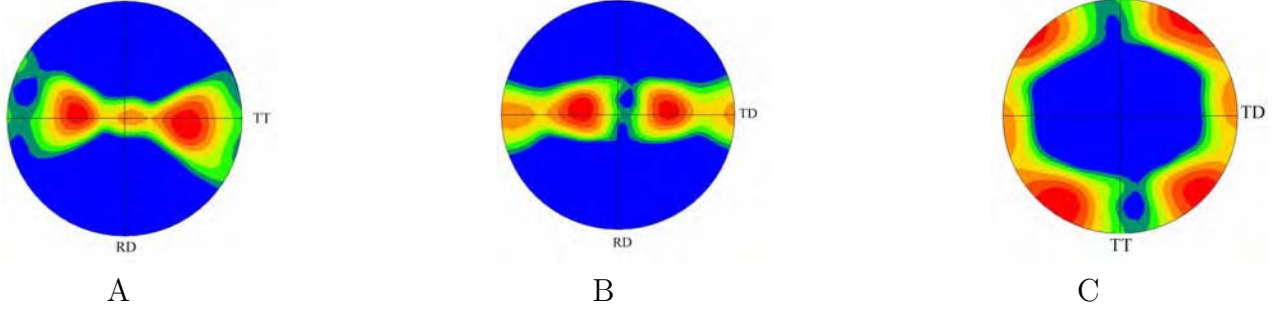


Figure 3: (0001) pole figures measured by neutron diffraction showing the initial texture in  $\alpha$ -titanium used in this study. The rolling directions (RD) and transverse direction (TD) are in the plane of the disk, while TT designates the the through thickness direction, normal to the plate. In A), TD direction is in the center and TT direction is side to side, in B), TT direction is in the center and TD direction side to side, while in C), RD is in the center and TD side to side.

A specialized miniature test specimen was used for the through-thickness (TT) tensile tests (Figure 5). In order to examine the microstructural evolution, tests were carried out to approximately 10%, 20%, 30%, 40% strains respectively or until complete failure of the specimen occurred. Deformed samples were thereafter examined by OIM. The uniaxial tensile test re-

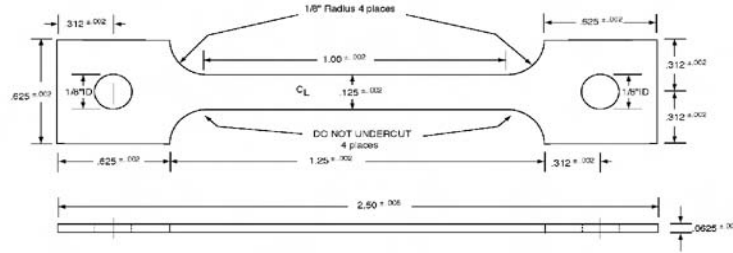


Figure 4: Geometry and dimensions of the specimens used for in-plane uniaxial tensile testing.

sults (Figure 6) show that the material displays orthotropic behavior. An anisotropy ratio for initial yield stress defined by the ratio of the yield stress in the through-thickness direction (the largest) to that in the transverse direction (the smallest value) is 1.27. In all tension tests, shear-type fracture was observed. In contrast, tensile fracture of magnesium alloy AZ31B, which also has HCP crystal structure is brittle (see data by [35]). To examine the effect of loading orientation on the mechanical response, cylindrical compression specimens ( 7.62 mm x 7.62 mm) were machined such that the axes of the cylinders were either along an in-plane (IP) or through-thickness (TT) plate directions (see Figure 4). Compression testing was conducted using an Instron 100 kN load cell and an Instron extensometer model number G-51-17-A with a gauge length of 12.7 mm. The uniaxial compression results (Figure 7) show an initial yield stress anisotropy ratio of 1.18, which is smaller than in tension. This observed variation



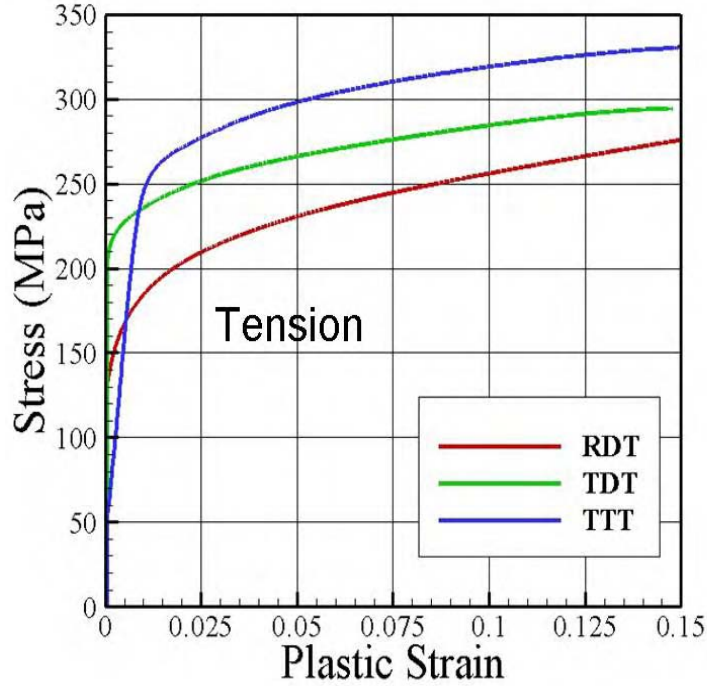


Figure 6: Uniaxial tensile tests results along the rolling (RDT), transverse (TDT), and through-thickness direction (TT)

Comparison between quasi-static test results in monotonic uniaxial compression and tension along the through-thickness direction are shown in Figure 12. A strong tension/compression asymmetry in initial yielding is observed whereas the asymmetry in hardening evolution is less pronounced. Since compressive loading is applied essentially perpendicular to the basal plane, in principle deformation twinning should be favored over non-basal slip. However, OIM measurements have shown very little twinning activity. To further elucidate the role of the deformation mechanisms on the macroscopic response for each loading direction and evaluate the evolution of anisotropy, post-test texture measurements were conducted using neutron diffraction.

### 2.2.1 Microstructure evolution during uniaxial compression deformation

The (0001) pole figure of the specimen deformed to 10%, 20%, 30% and 40% strains in uniaxial compression along the rolling direction are shown Figures 13 to 14. A significant texture evolution is observed. Note that at 20% strain the  $c$ -axis of most of the grains has flipped by  $90^\circ$ , which correlates with the OIM post-test analysis. Figure 15 shows these same pole figures at the appropriate strain levels on the stress-strain curve. It is clear that the point on

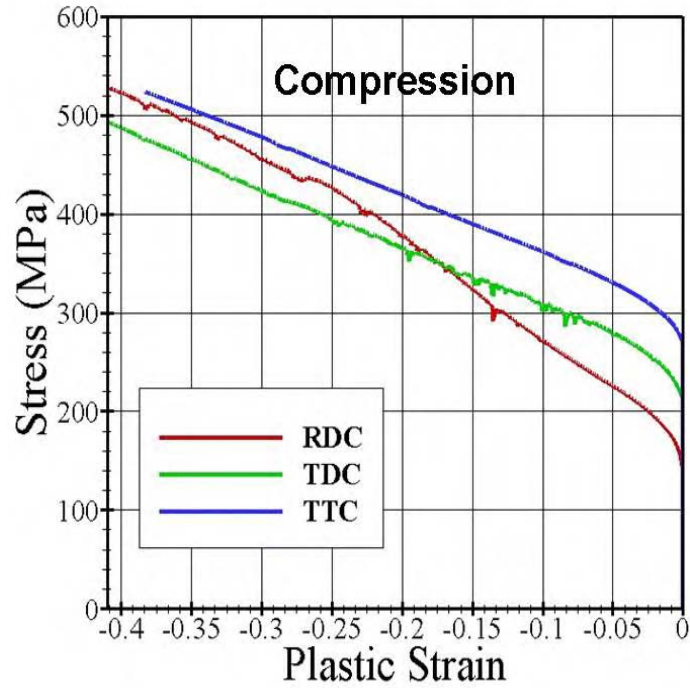


Figure 7: Uniaxial compression tests results along the rolling (RDT), transverse (TDT), and through-thickness direction (TTT).

the stress-strain curve at which there is an abrupt change in hardening rate corresponds to the same strain level at which a strong texture evolution is observed. Figures 16 and 17 show the (0001) pole figures for the specimens loaded in uniaxial compression in the transverse direction to strains of 10%, 20%, 30% and 40%, respectively. Note the fairly strong alignment of the c-axis in most of the grains with the through-thickness (TT) direction. Owing to the basal texture of the material, the compressive flow stress in the through-thickness direction is larger than in the in-plane orientations. This is also revealed by the uniaxial loading tests which show that the plate is stronger in the transverse direction than in the rolling direction. Note that there is only a slight texture evolution indicating that deformation twinning may not be a dominant deformation mechanisms for this loading path.

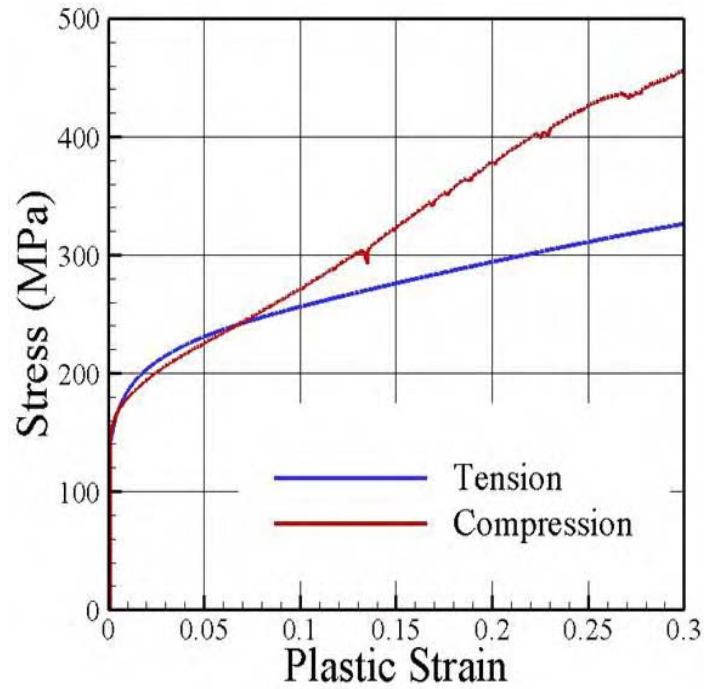


Figure 8: Comparison between the compression and tension uniaxial response in the rolling direction.



Figure 9: Orientation Imaging Microscopy map showing the evidence of twins (in red) in the specimen deformed to 10% strain in simple compression along the rolling direction. The twin volume fraction is 17%.



Figure 10: Orientation Imaging Microscopy map showing significant twinning activity (45% volume fraction) in the  $\alpha$ -titanium sample deformed to 20% strain in simple compression along the rolling direction.

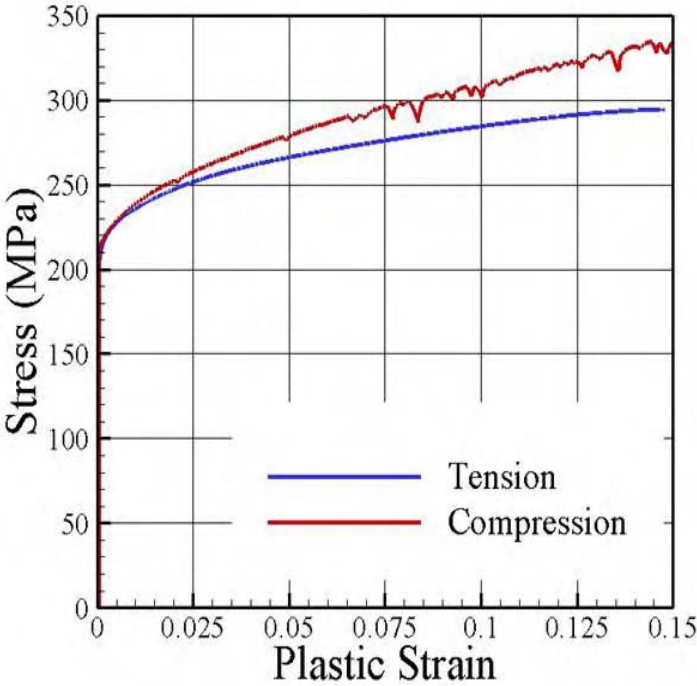


Figure 11: Comparison between the compression and tension uniaxial response in the transverse direction.

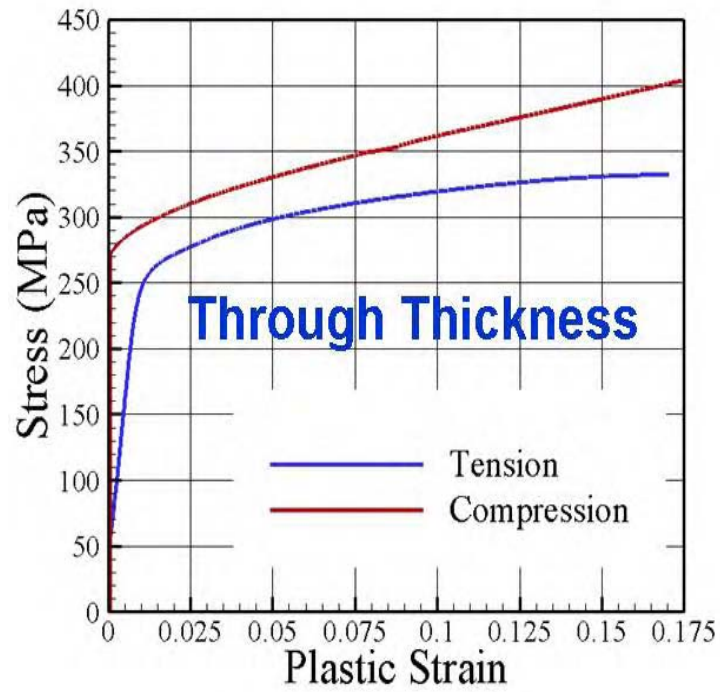


Figure 12: Comparison between the compression and tension uniaxial response in the through-thickness direction.

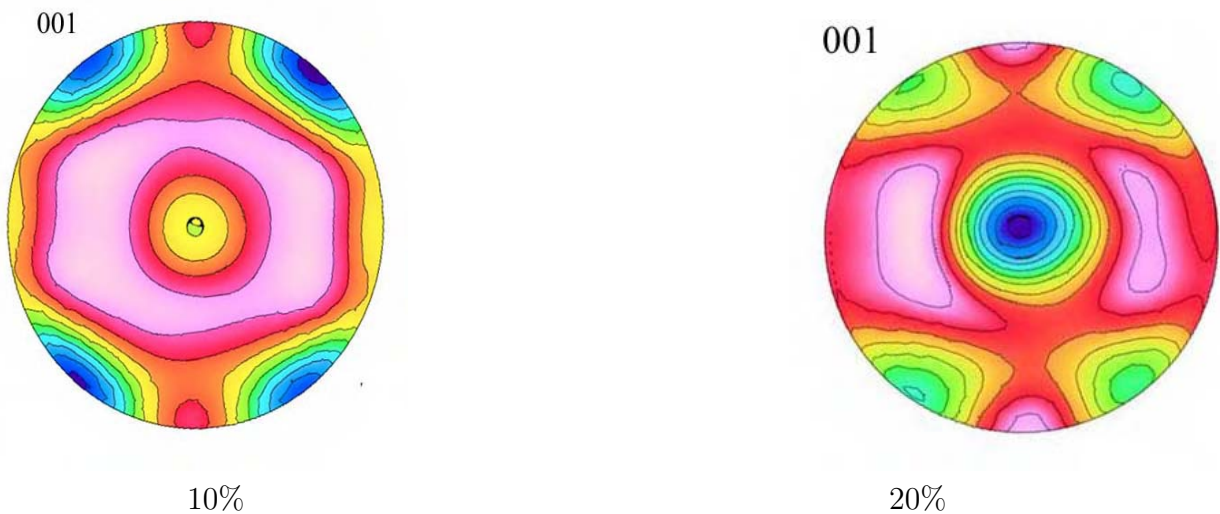


Figure 13: Measured (0001) pole figures for specimens loaded in compression to 10 and 20% in the rolling direction (RD in center and the TD direction from side to side).

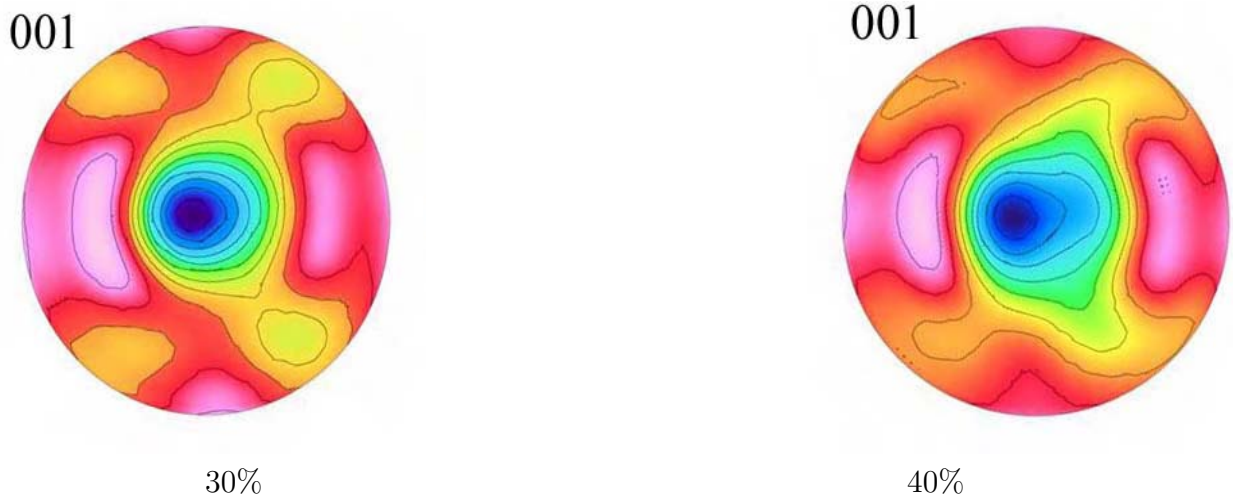


Figure 14: Measured (0001) pole figures for specimens loaded in compression to 30 and 40 % strain in rolling direction (RD in center and the TD direction from side to side).

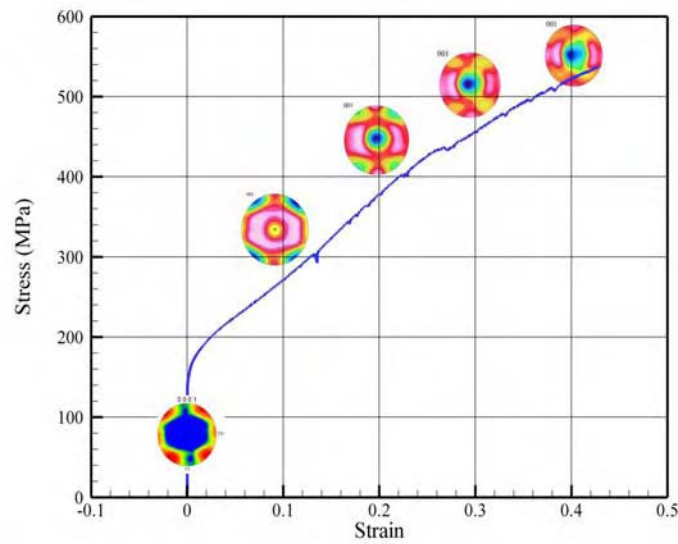


Figure 15: Texture evolution for compressive loading in the rolling direction

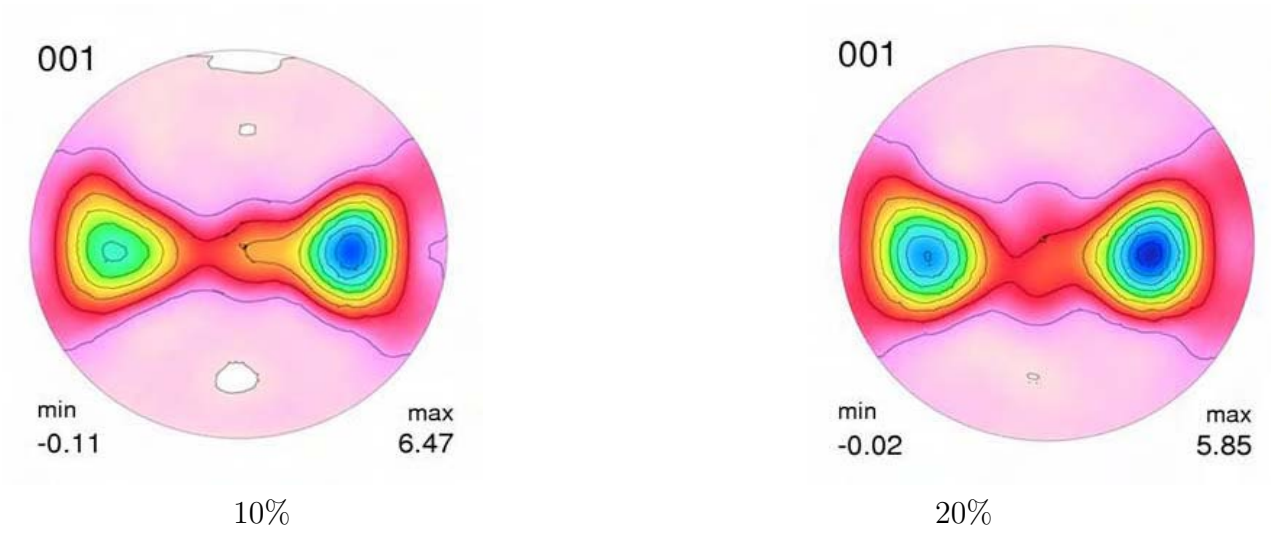


Figure 16: (0001) pole figure for specimens loaded in compression to 10% and 20% in the transverse direction, respectively (TD in center and the TT from side to side).

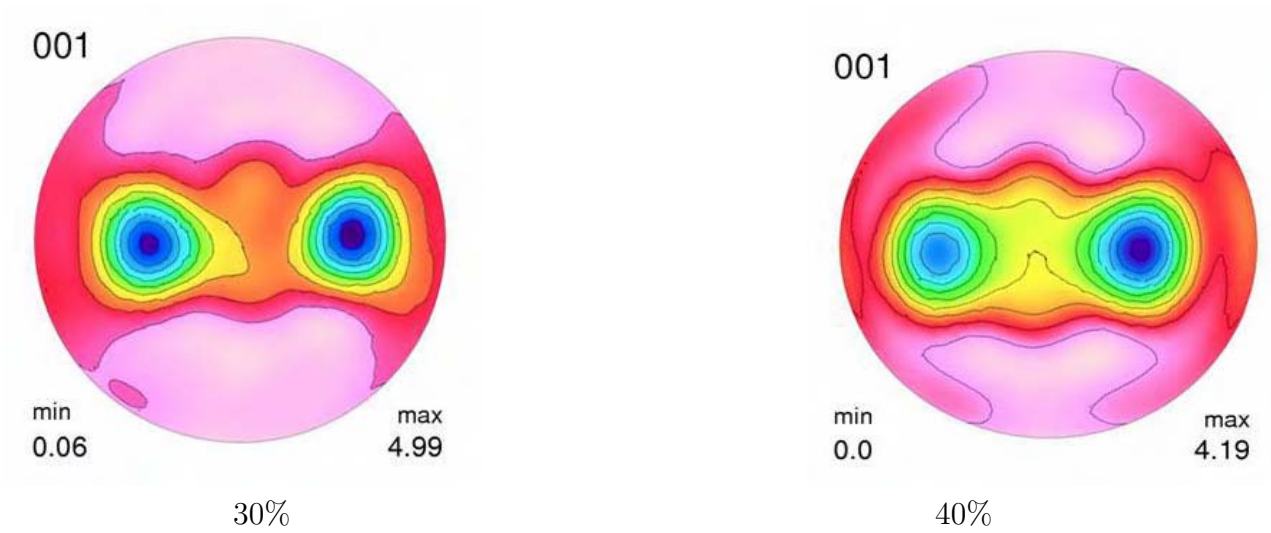


Figure 17: (0001) pole figure for specimens loaded in compression to 30 % and 40 % strain in transverse direction; TD in center and the TT from side to side

Figures 18 and 19 show there is only a slight texture evolution in uniaxial compression in the through-thickness direction indicating only minimal twinning for this loading path.

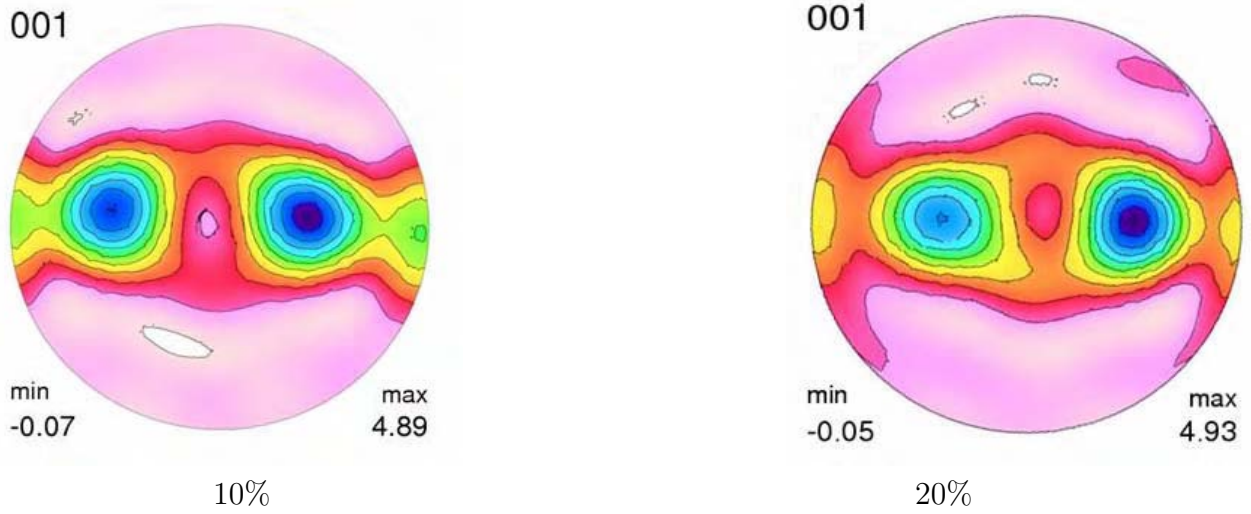


Figure 18: (0001) pole figure for specimens loaded in compression in through thickness direction to 10 % and 20 % strain, respectively; TT in center and the TD direction from side to side

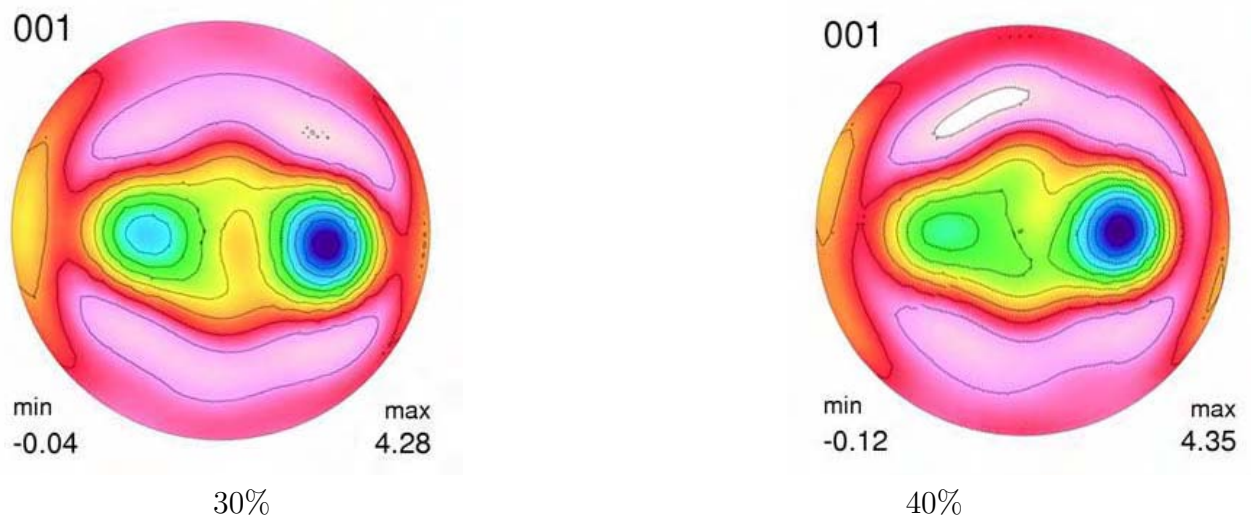


Figure 19: (0001) pole figure for specimens loaded in compression in the through-thickness direction up to 30% and 40 % strain, respectively; TT in center and the TD direction from side to side

Figure 20 and Figure 21 show these same pole figures at the appropriate strain levels on the stress-strain curve for TD compression and TT compression, respectively. It is clear that twinning is not a dominant mechanisms for these loading paths. There are no abrupt changes in hardening rate. This correlates with the texture measurements that indicate minimal grain rotations during deformation. As outlined in the introduction, the mechanical response and deformation mechanisms of high-purity  $\alpha$ - titanium have been reported only for monotonic simple compression in the through-thickness direction, plane strain compression, or simple shear. The texture measurements reported here expand the existing knowledge base by providing a thorough characterization of the anisotropy of the mechanical response and its evolution during monotonic loading. Post test analysis using OIM has shown that significant twinning activity occurs only in rolling direction compression.

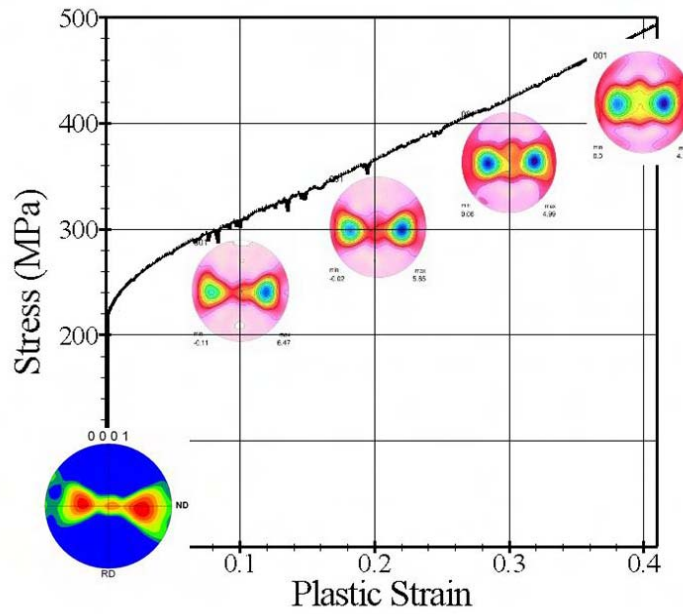


Figure 20: Texture evolution for compressive loading in the transverse direction.

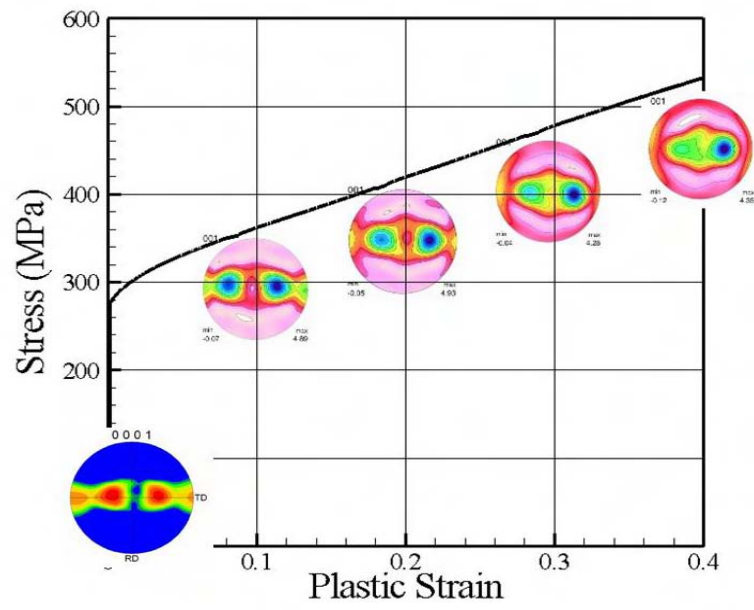


Figure 21: Texture evolution for compressive loading in the through thickness direction.

### 2.2.2 Four-Point Beam Bending Test Results

In order to provide validation data for the modeling effort, four-point bending tests were conducted. The specimens were beams of length 57.15 mm with a square cross section of 6.35 mm as shown in Figure 22 (A). The uniaxial and compression tests have revealed that the tension-compression asymmetry of the material is highly directional. Thus, to further characterize this tension-compression asymmetry by bending testing, it is necessary to carry out tests for at least four test configurations and loading scenarios. To this end, four beam samples were cut. Two samples were machined such that the long axis was along the RD while the other two samples were machined with the long axis along the TD. For each of these two sets of specimens, one beam was loaded in the through- thickness direction while the other sample was loaded in the in-plane direction normal to the beam axis. These four test configurations are shown in Figure 22 (B). To simplify the notations when describing the beam test results, we denote by  $(x, y, z)$  the reference frame associated to the three orthotropic axes with  $x = \text{RD}$ ,  $y = \text{TD}$ , and  $z = \text{TT}$ . The testing jig with a test specimen is shown in Figure 23. The two upper pins were dis-

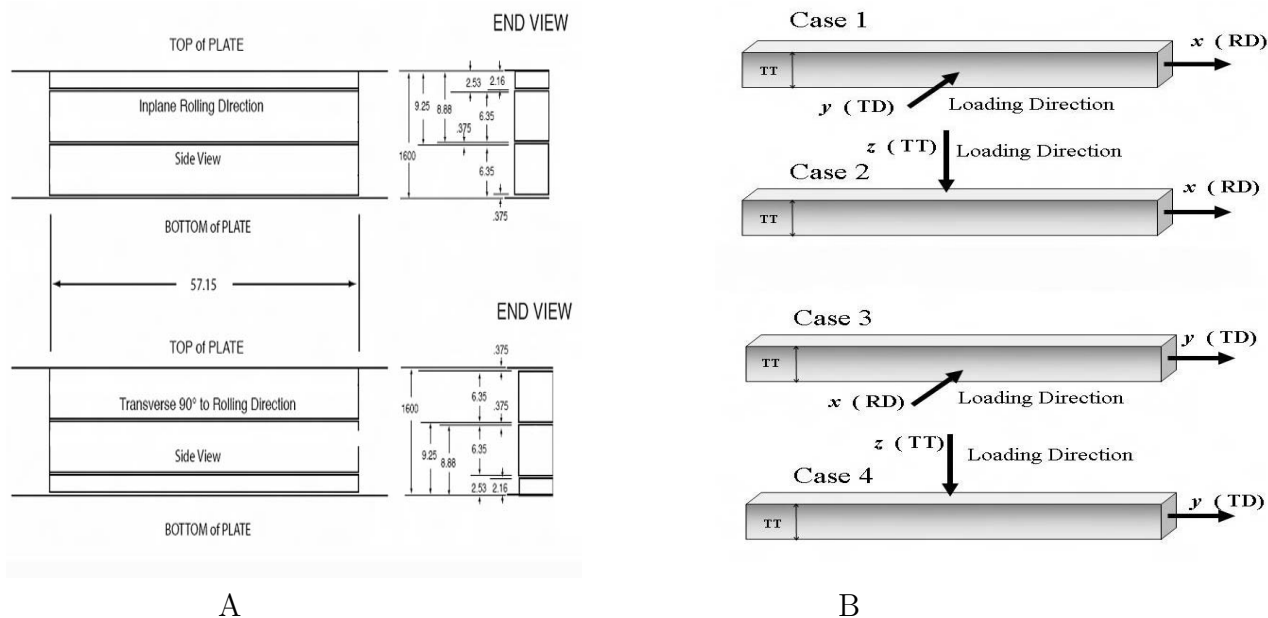
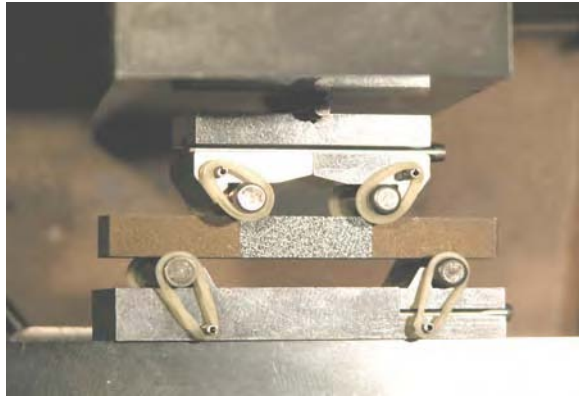
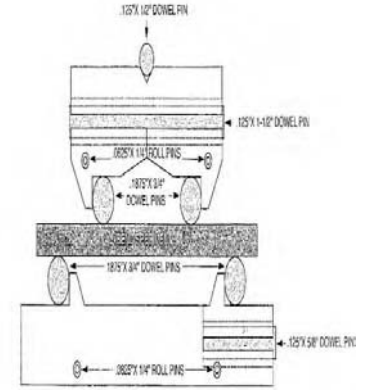


Figure 22: Four-point bending test specimens: A) Specimen dimensions; B) Orientation definitions: in Case 1 and Case 2 the long axis of the beam is aligned with the rolling direction ( $x$ ) while in Case 3 and Case 4 the long axis of the beam is aligned with the transverse direction ( $y$ ).

placement controlled to approximately 5.5 mm. A typical load pin displacement path is shown in Figure 24. Along one side of each beam, a speckle pattern was sprayed and digital image correlation (DIC) (see [42, 43]) was used to determine the strain field after deformation. The image taken had 88 pixels along the short direction of the beam. The beam dimension in that direction is 6.35 mm. Thus, the physical distance between pixels is 72 micron/pixel. The DIC



A



B

Figure 23: Four point beam test jig: A) with test specimen; B) dimensions and pin positions.

method can detect displacements of 0.01 pixel, therefore the error is less than  $1 \mu\text{m}$ . A typical undeformed and deformed grid are shown in Figure 25. Note that the grid and subsequently measured strain field do not cover the entire speckle field. Also, the deformed specimens were cut at the midpoint along their axis to examine the final deformed cross section. Measurements at this cross section were taken for comparison to the FE simulations. A contour plot of the experimental axial strain field for each of the loading scenarios (see Figure 22) are shown in Figures 26 to 29. The axial strain is defined as the strain in the long axis direction of the specimen. For Case 1 and Case 2 loadings, the long axis is along the rolling direction  $x$  so the axial strain component is  $\varepsilon_x$  while for the Case 3 and Case 4, the long axis corresponds to the transverse direction  $y$ , therefore the axial strain is  $\varepsilon_y$ . In all tests, some non-uniform deformation occurred in the direction normal to the plane for which the data were reported, thus introducing a slight error in the computation of the axial strains using the DIC methodology.

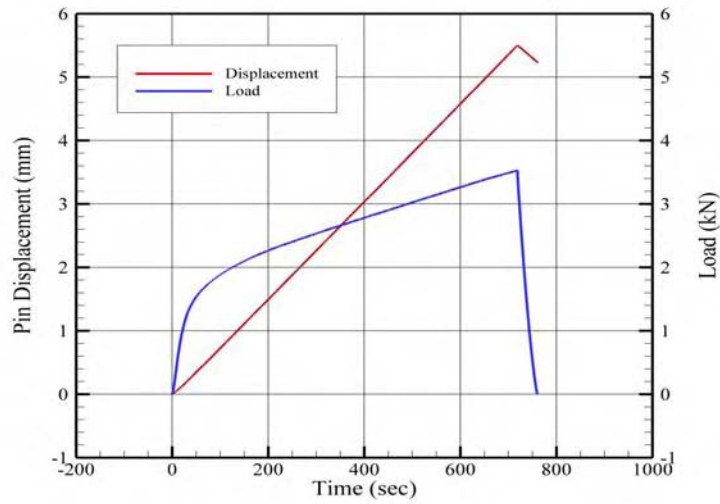


Figure 24: Typical load vs displacement curve in bending: the left vertical axis indicates the pin displacement (in mm), the right vertical axis represents the applied load (in kN), time (in sec) is plotted on the horizontal axis.

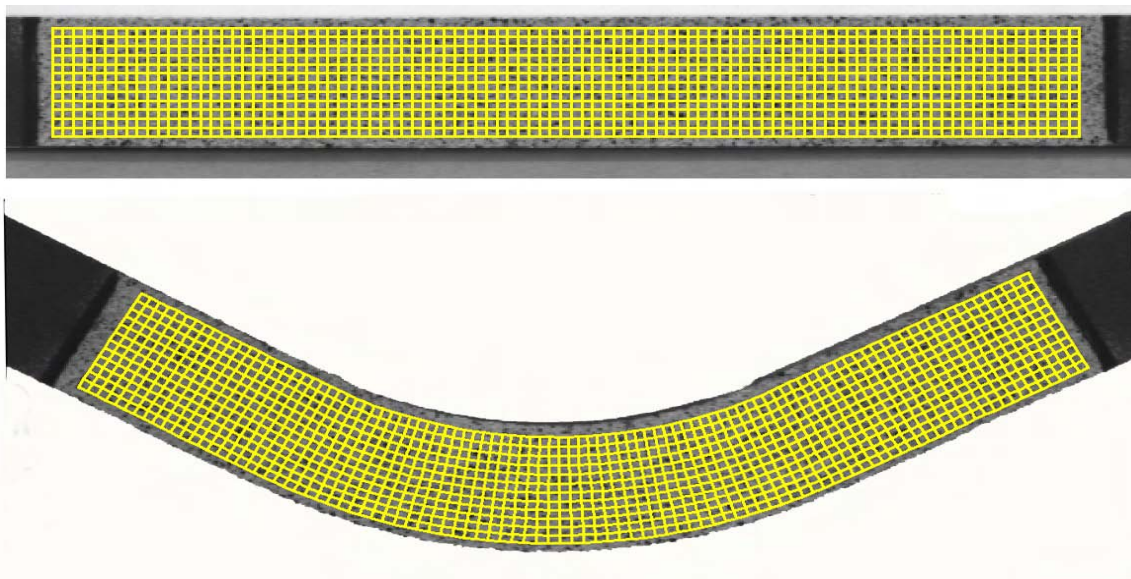


Figure 25: Typical undeformed and deformed beam grid pattern used with digital image correlation (DIC ) for generating the experimental strain field.

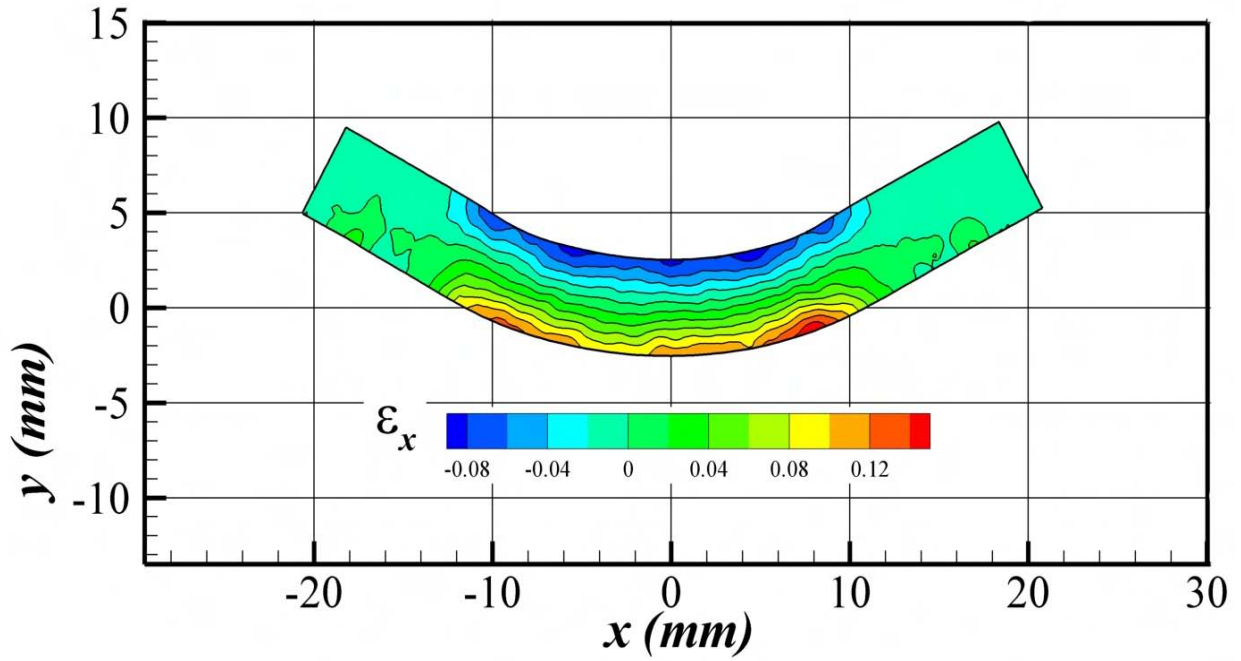


Figure 26: Experimental axial strain ( $\epsilon_x$ ) fields for Case 1 configuration: long axis in  $x$ =RD, loading in  $y$ =TD.

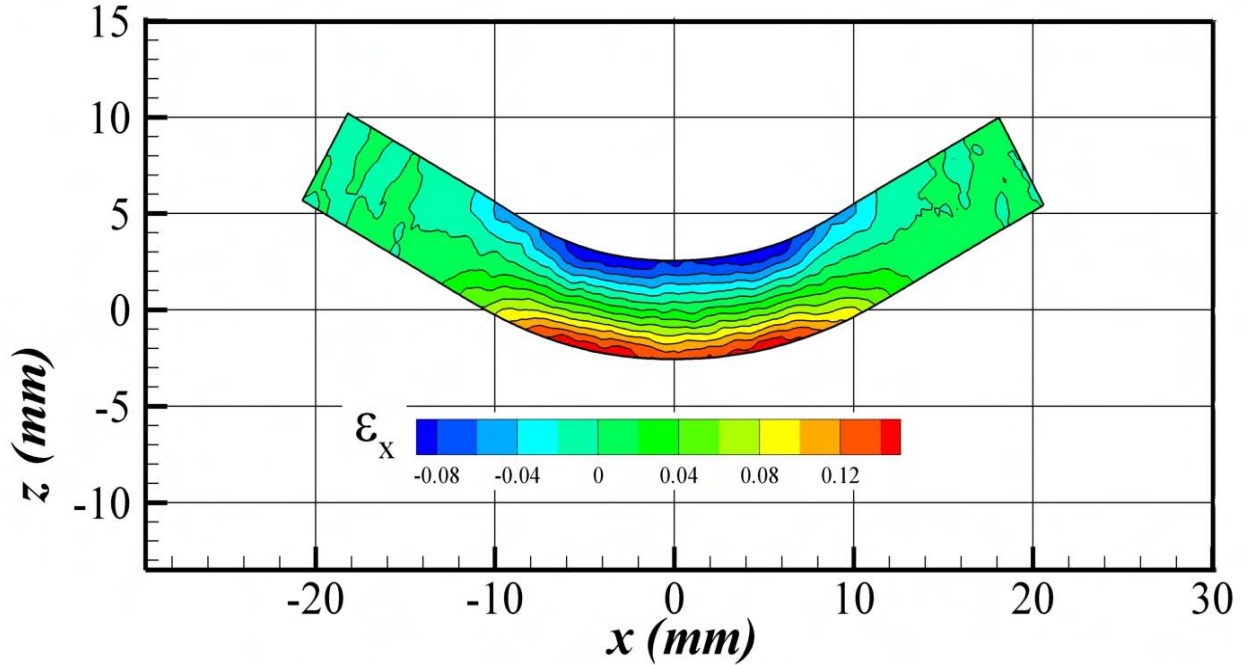


Figure 27: Experimental axial strain ( $\epsilon_x$ ) fields for Case 2 configuration: Long axis in  $x$ =RD, loading in  $z$ =TT.

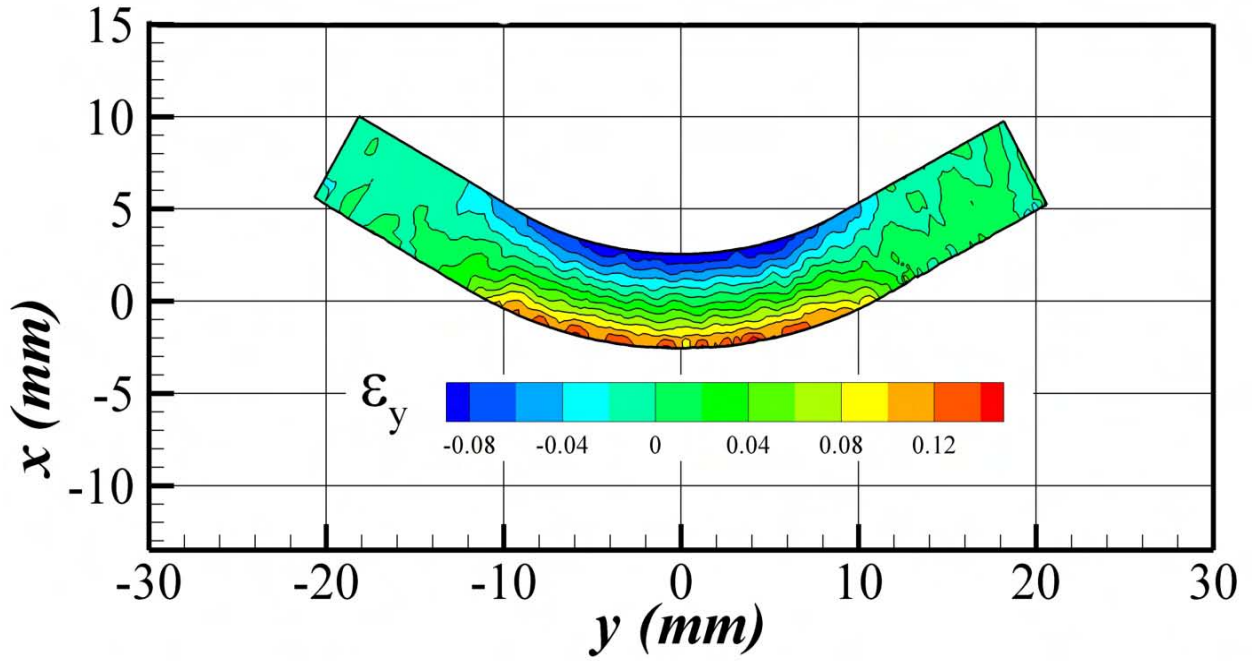


Figure 28: Experimental axial strain ( $\epsilon_y$ ) fields for Case 3 configuration: Long axis in  $y=TD$ , loading in  $x=RD$ .

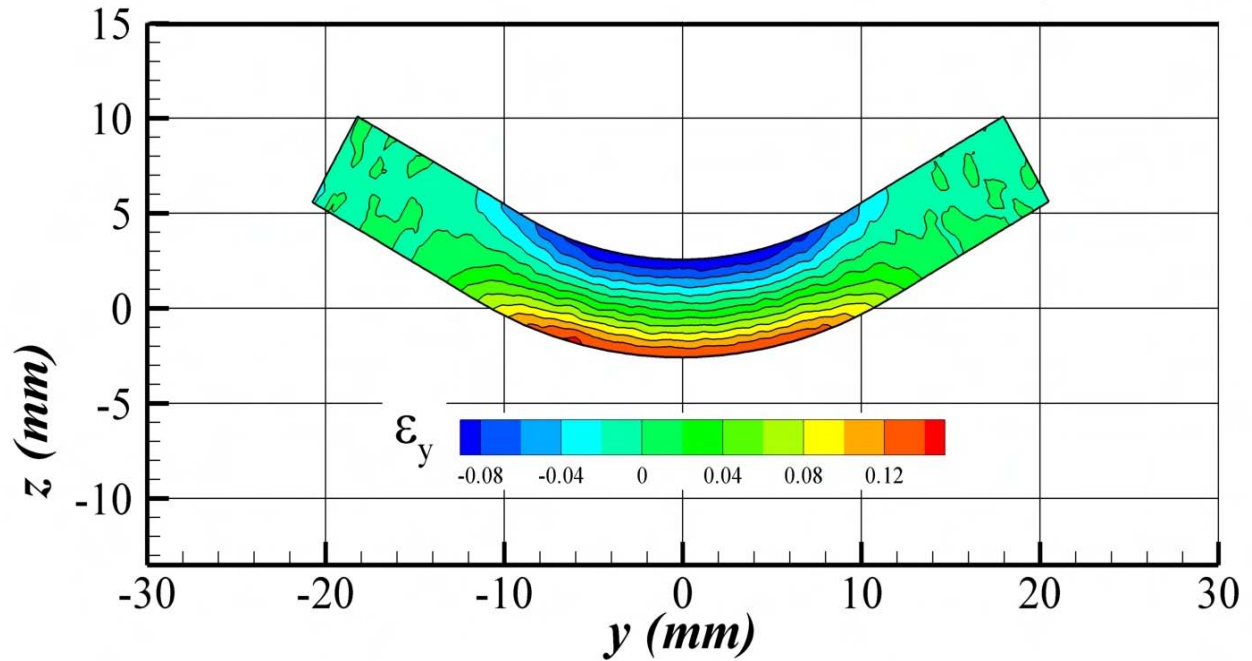


Figure 29: Experimental axial strain ( $\epsilon_y$ ) fields for Case 4 configuration: Long axis in  $y=TD$ , loading in  $z=TT$ .

### 3 Proposed model for description of the elastic-plastic deformation of high-purity $\alpha$ -titanium

To model the behavior of the high purity  $\alpha$ - titanium material in the quasi-static loading regime, an elastic-plastic modeling approach is adopted. To describe the onset of yielding, an anisotropic yield criterion that captures both strength differential effects and the anisotropy in yielding will be developed. A parameter identification procedure based on experimental results will be also outlined. The integration algorithm for the proposed model, and its implementation in the explicit FE code EPIC follows. Comparison between model predictions and the data in uniaxial loading is given in Section 3.5. Validation of the model through its application to the description of the bending response is presented in Section 3.6.

#### 3.1 Proposed yield criterion

One of the goals of this research is to advance the current state-of-the-art by developing user-friendly, micro-structurally based and numerically robust macroscopic constitutive models that can capture with accuracy the particularities of the plastic response of hexagonal metals, in particular high purity  $\alpha$ -titanium. A full three-dimensional anisotropic yield criterion is proposed. Key in this development is the use of the isotropic yield function developed in [24] that captures tension/compression asymmetries. First, a brief overview of this yield criterion is given. After reviewing the general aspects of linear transformation operating on the Cauchy stress tensor, the anisotropic yield function is developed. The input data needed for the calculation of the anisotropic yield function coefficients are then discussed.

##### 3.1.1 Isotropic yield function

If the deformation mechanism of plastic deformation is sensitive to the sign of the stress as is the case of deformation twinning, the isotropic yield function ought to be represented by an odd function in the principal values of the stress deviator. To describe the asymmetry in yielding, due to twinning, Cazacu and Barlat [24] proposed an isotropic yield criterion of the form

$$f = J_2^{\frac{3}{2}} - cJ_3 = \tau_Y^3 \quad (1)$$

where  $\tau_Y$  is the yield stress in pure shear and  $c$  is a material parameter;  $J_2$  and  $J_3$  are the second and third invariants of the stress deviator, respectively. The constant  $c$  can be expressed in terms of the yield in uniaxial tension,  $\sigma_T$ , and the yield in uniaxial compression,  $\sigma_C$ , as

$$c = \frac{3\sqrt{3}(\sigma_T^3 - \sigma_C^3)}{2(\sigma_T^3 + \sigma_C^3)} \quad (2)$$

If  $\sigma_T = \sigma_C$ , then  $c = 0$ , and the isotropic criterion (1) reduces to the von Mises yield criterion. To ensure convexity,  $c$  is limited to the following range:  $c \in [-3\sqrt{3}/2, 3\sqrt{3}/4]$ . In principal stress

space and for plane stress conditions, the yield locus is expressed as

$$\frac{1}{3} (\sigma_1^2 - \sigma_1\sigma_2 + \sigma_2^2)^{\frac{3}{2}} - \frac{c}{27} [2\sigma_1^3 + 2\sigma_2^3 - 3(\sigma_1 + \sigma_2)\sigma_1\sigma_2] = \sigma_Y^3 \quad (3)$$

When  $c \neq 0$ , this yield locus is a triangle with rounded corners. As an example, in Figure 30 is shown the yield locus (3) corresponding to three different ratios of  $\sigma_T/\sigma_C$ . When  $\sigma_T/\sigma_C$  is one, the yield locus reduces to the von Mises ellipse.

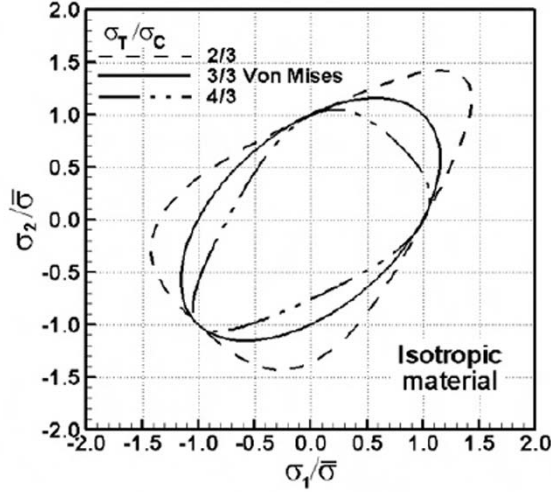


Figure 30: Plane stress yield loci (3) for various values of the yield stress ratio  $\sigma_T/\sigma_C$ .

Figure 31 shows a comparison between the predictions according to the the yield criterion (1) and results of polycrystalline simulations for randomly oriented FCC (solid circles) and BCC (open circles) polycrystals obtained by Hosford and Allen [25] using a generalization of the Taylor-Bishop model [49]. In the polycrystalline model [25] it was assumed that the only deformation mechanism is twinning. According to this polycrystalline model, for FCC randomly oriented polycrystals the ratio  $\sigma_T/\sigma_C$  is 0.78 which corresponds to a value of  $c$  equal to 0.92 (see (2) ) while for a randomly oriented BCC polycrystal this ratio is of 1.28, hence the value of  $c$  is  $-0.92$ . It is clear that the analytic criterion (1) describes very well the asymmetry in yielding resulting from activation of twinning. Next, in order to describe both the asymmetry in yielding due to twinning and the anisotropy of rolled sheets, an extension to orthotropy of the isotropic criterion given by(1)is developed.

### 3.2 Proposed orthotropic criterion

An extension to orthotropy of the isotropic criterion (1) can be obtained by using a linear transformation approach. This method consists in replacing in the expression of the isotropic criterion (1) the Cauchy stress,  $\boldsymbol{\sigma}$  by  $\boldsymbol{\Sigma} = \mathbf{L}\boldsymbol{\sigma}$ , where  $\mathbf{L}$  is a  $4^{th}$  order tensor. Thus, the anisotropic criterion is of the form

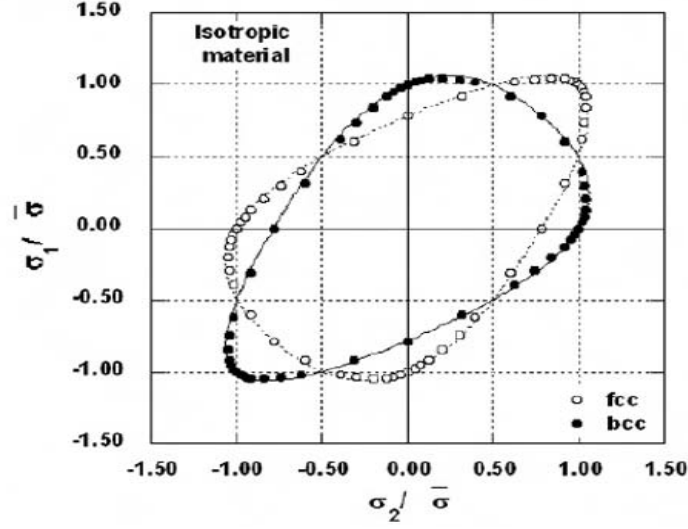


Figure 31: Comparison between plane stress yield surfaces (with  $\sigma_3 = 0$ ) according to Cazacu and Barlat [24] and polycrystalline model of Hosford and Allen [25] for randomly oriented BCC polycrystals ( $c = 0.92$ ); and FCC randomly oriented polycrystals ( $c = -0.92$ ).

$$f^o = \left[ \frac{1}{2} \text{tr}(\Sigma^2) \right]^{3/2} - \frac{c}{3} \text{tr}(\Sigma^3) = \tau_Y^3 \quad (4)$$

In the above equation  $\tau_Y$  denotes the pure shear yield stress. The tensor  $\mathbf{L}$  satisfies: (a) the symmetry conditions:  $L_{ijkl} = L_{jikl} = L_{jilk} = L_{klij}$  ( $i, j, k, l = 1 \dots 3$ ), (b) the requirement of invariance with respect to the symmetry group of the material, and (c)  $L_{1k} + L_{2k} + L_{3k} = 0$  for  $k = 1, 2$ , and  $3$ , which ensures that  $\Sigma$  is traceless and consequently yielding is independent of hydrostatic pressure. Relative to the orthotropy axes  $(x, y, z)$ ,  $\mathbf{L}$  is represented by

$$\mathbf{L} = \begin{bmatrix} \frac{(a_2+a_3)}{3} & -\frac{a_3}{3} & -\frac{a_2}{3} & 0 & 0 & 0 \\ -\frac{a_3}{3} & \frac{(a_1+a_3)}{3} & -\frac{a_1}{3} & 0 & 0 & 0 \\ -\frac{a_2}{3} & -\frac{a_1}{3} & \frac{(a_1+a_2)}{3} & 0 & 0 & 0 \\ 0 & 0 & 0 & a_4 & 0 & 0 \\ 0 & 0 & 0 & 0 & a_5 & 0 \\ 0 & 0 & 0 & 0 & 0 & a_6 \end{bmatrix}$$

where  $a_i$ ,  $i=1 \dots 6$  are constants. In the  $(x, y, z)$  frame,  $x$  represents the rolling direction,  $y$  the transverse direction, and  $z$  the thickness direction. Thus, in the  $(x, y, z)$  frame the transformed stress tensor,  $\Sigma$ , is given by :

$$\Sigma = \begin{bmatrix} \frac{1}{3}[(a_2 + a_3)\sigma_x - a_3\sigma_y - a_2\sigma_z] & a_4\tau_{xy} & a_5\tau_{xz} \\ a_4\tau_{xy} & \frac{1}{3}[-a_3\sigma_x + (a_1 + a_3)\sigma_y - a_1\sigma_z] & a_6\tau_{yz} \\ a_5\tau_{xz} & a_6\tau_{yz} & \frac{1}{3}[-a_2\sigma_x - a_1\sigma_y + (a_1 + a_2)\sigma_z] \end{bmatrix}$$

Let  $J_2^o = [\frac{1}{2}tr(\Sigma^2)]$  and  $J_3^o = \frac{1}{3}tr(\Sigma^3)$ .

Note that  $J_2^o$  is an extension to orthotropy of  $J_2$ , the second invariant of the stress deviator, while  $J_3^o$  is an orthotropic extension of  $J_3$ , the third invariant of the Cauchy stress deviator. In the symmetry frame,  $(x, y, z)$ , these generalized invariants are expressed in terms of the Cauchy stress  $\sigma$  as

$$\begin{aligned} J_2^o = & \frac{1}{9} [ (a_2^2 + a_3^2 + a_2a_3) \sigma_x^2 \\ & + (a_1^2 + a_3^2 + a_1a_3) \sigma_y^2 \\ & + (a_1^2 + a_2^2 + a_1a_2) \sigma_z^2 \\ & + (-2a_3^2 + a_1a_2 - a_1a_3 - a_2a_3) \sigma_x\sigma_y \\ & + (-2a_2^2 - a_1a_2 + a_1a_3 - a_2a_3) \sigma_x\sigma_z \\ & + (-2a_1^2 - a_1a_2 - a_1a_3 + a_2a_3) \sigma_y\sigma_z ] \\ & + a_4^2\tau_{xy}^2 + a_5^2\tau_{xz}^2 + a_6^2\tau_{yz}^2 \end{aligned} \quad (5)$$

$$\begin{aligned} J_3^o = & \frac{1}{27} [ (a_2^2a_3 + a_2a_3^2) \sigma_x^3 + (a_1^2a_3 + a_3^2a_1) \sigma_y^3 + (a_1^2a_2 + a_1a_2^2) \sigma_z^3 \\ & + (-a_1a_2^2 + a_1a_3^2 - a_2^2a_3 - 2a_2a_3^2) \sigma_x^2\sigma_y \\ & + (a_1a_2^2 - a_1a_3^2 - a_2^2a_3 - 2a_2a_3^2) \sigma_x^2\sigma_z \\ & + (-a_1^2a_2 - a_1^2a_3 + a_2a_3^2 - 2a_1a_3^2) \sigma_y^2\sigma_x \\ & + (a_1^2a_2 - 2a_1^2a_3 - a_1a_3^2 - a_2a_3^2) \sigma_y^2\sigma_z \\ & + (-a_1^2a_2 - a_1^2a_3 - 2a_1a_2^2 + a_2^2a_3) \sigma_z^2\sigma_x \\ & + (-2a_1^2a_2 + a_1^2a_3 - a_1a_2^2 - a_2^2a_3) \sigma_z^2\sigma_y \\ & + 2(a_1^2a_2 + a_1^2a_3 + a_2^2a_1 + a_2^2a_3 + a_3^2a_1 + a_3^2a_2) \sigma_x\sigma_y\sigma_z ] \\ & + \frac{1}{3} \{ [a_2a_4^2\sigma_x + a_1a_4^2\sigma_y - (a_1a_4^2 + a_2a_4^2) \sigma_z] \tau_{xy}^2 \\ & + [a_3a_5^2\sigma_x - (a_1a_5^2 + a_3a_5^2) \sigma_y + a_1a_5^2\sigma_z] \tau_{xz}^2 \\ & + [(-a_2a_6^2 - a_3a_6^2) \sigma_x - a_3a_6^2\sigma_y + a_2a_6^2\sigma_z] \tau_{yz}^2 \} \\ & + 2a_4a_5a_6\tau_{xy}\tau_{xz}\tau_{yz} \end{aligned} \quad (6)$$

For plane stress, the expressions of these generalized invariants reduce to

$$\begin{aligned} J_2^o = & \frac{1}{9} [ (a_2^2 + a_3^2 + a_2a_3) \sigma_x^2 + (a_1^2 + a_3^2 + a_1a_3) \sigma_y^2 \\ & + (-2a_3^2 + a_1a_2 - a_1a_3 - a_2a_3) \sigma_x\sigma_y ] + a_4^2\tau_{xy}^2 \end{aligned} \quad (7)$$

$$\begin{aligned}
J_3^o &= \frac{1}{27} \left[ (a_2^2 a_3 + a_2 a_3^2) \sigma_x^3 + (a_1^2 a_3 + a_3^2 a_1) \sigma_y^3 + \right. \\
&\quad + (-a_1 a_2^2 + a_1 a_3^2 - a_2^2 a_3 - 2a_2 a_3^2) \sigma_x^2 \sigma_y \\
&\quad + (-a_1^2 a_2 - a_1^2 a_3 + a_2 a_3^2 - 2a_1 a_3^2) \sigma_y^2 \sigma_x \left. \right] \\
&\quad + \frac{1}{3} (a_2 a_4^2 \sigma_x \tau_{xy}^2 + a_1 a_4^2 \sigma_y \tau_{xy}^2)
\end{aligned} \tag{8}$$

Hence, the proposed orthotropic yield condition is

$$(J_2^o)^{3/2} - c J_3^o = \tau_Y^3 \tag{9}$$

The anisotropy coefficients  $a_i$  and the strength differential parameter  $c$  involved in the proposed anisotropic criterion (9) can be determined based on uniaxial tensile and compressive tests along different orientations  $\theta$  with respect to the rolling direction  $x$ . In particular, if  $R_{tens}$  and  $R_{comp}$  denote the yield stress in tension and compression along the rolling direction, respectively, then according to (9)

$$R_{tens} = \frac{\tau_Y}{3} \left\{ (a_2^2 + a_3^2 + a_2 a_3)^{\frac{3}{2}} - c (a_2^2 a_3 + a_3^2 a_2) \right\}^{-\frac{1}{3}} \tag{10}$$

$$R_{comp} = \frac{\tau_Y}{3} \left\{ (a_2^2 + a_3^2 + a_2 a_3)^{\frac{3}{2}} + c (a_2^2 a_3 + a_3^2 a_2) \right\}^{-\frac{1}{3}} \tag{11}$$

Similarly, if  $T_{tens}$  and  $T_{comp}$  denote the yield stress in tension and compression along the transverse direction,  $y$ , then the model predicts that

$$T_{tens} = \frac{\tau_Y}{3} \left\{ (a_1^2 + a_3^2 + a_1 a_3)^{\frac{3}{2}} - c (a_1^2 a_3 + a_3^2 a_1) \right\}^{-\frac{1}{3}} \tag{12}$$

$$T_{comp} = \frac{\tau_Y}{3} \left\{ (a_1^2 + a_3^2 + a_1 a_3)^{\frac{3}{2}} + c (a_1^2 a_3 + a_3^2 a_1) \right\}^{-\frac{1}{3}} \tag{13}$$

When  $\sigma_1 = \sigma_2 = \sigma_b^T$  and  $\sigma_3 = 0$  (equibiaxial loading), according to the proposed model yielding occurs when

$$\sigma_b^T = \tau_Y \left[ (2a_1 - 2b_2 - b_3)^{3/2} - c \frac{a_1 a_2 (a_1 + a_2)}{27} \right]^{-\frac{1}{3}} \tag{14}$$

while under equibiaxial compression, i.e., for  $\sigma_1 = \sigma_2 = \sigma_b^C$

$$\sigma_b^C = \tau_Y \left[ (2a_1 - 2b_2 - b_3)^{3/2} + c \frac{a_1 a_2 (a_1 + a_2)}{27} \right]^{-\frac{1}{3}} \tag{15}$$

The anisotropy coefficients involved in the proposed orthotropic yield criterion can be determined by minimizing cost functions. The experimental data in the cost functions may consist of yielded stresses in tension and compression corresponding to different orientations in the plane of the plate and normal to the plane of the plate using the above equations. If available,  $r$ -value data can be used. If experimental data are not available for a given strain path, they can be substituted with numerical data obtained from polycrystalline calculations.

For the  $\alpha$ -titanium material studied, the coefficients of the model corresponding to fixed levels of accumulated plastic strain (up to 0.5) were determined using the measured tensile flow data at  $0^\circ$ ,  $45^\circ$ ,  $90^\circ$  and compressive flow data at  $0^\circ$  and  $90^\circ$ . In tensile loading, the specimens experienced uniform deformation up to about 20% strain, at which level localized deformation and necking occurred. Tensile data beyond 0.2 strain were obtained by extrapolation. The corresponding theoretical yield surfaces along with the experimental values (filled squares) are shown in Figure 32. Note that the proposed criterion matches the data very well. The

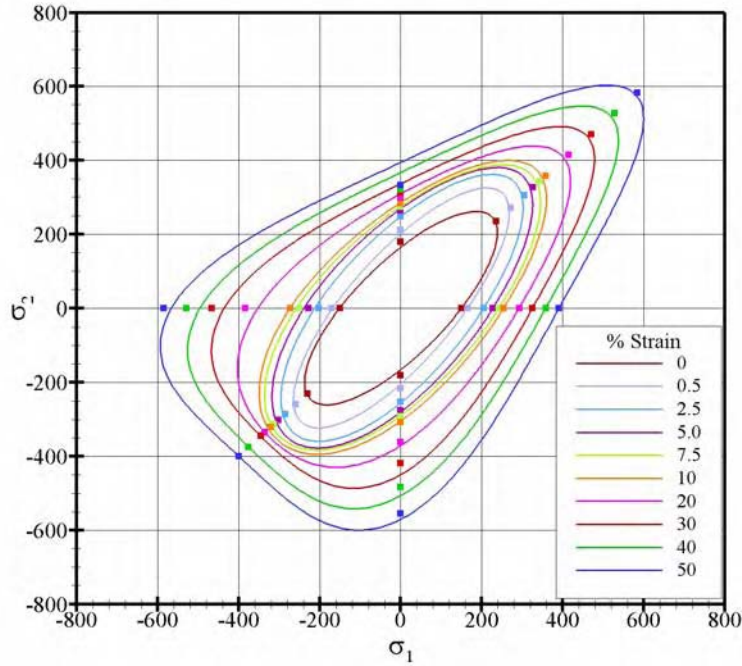


Figure 32: Theoretical yield surfaces according to Equation (9) and experimental data (symbols) corresponding to various strain levels

quadratic yield criterion of Hill [12] is the most widely used orthotropic yield criterion available and has proven to be accurate and robust for many materials, especially steels. However, it can not account for the strength differential observed in hexagonal materials. For comparison purposes, Hill's criterion is applied to the high purity titanium material used in this research. With respect to the orthotropy axes  $(x, y, z)$ , Hill [12] orthotropic yield criterion is written as

$$F(\sigma_y - \sigma_z)^2 + G(\sigma_z - \sigma_x)^2 + H(\sigma_x - \sigma_y)^2 + 2L\tau_{yz}^2 + 2M\tau_{zx}^2 + 2N\tau_{xy}^2 = 1 \quad (16)$$

where the coefficients  $F$ ,  $G$ ,  $H$ ,  $L$ ,  $M$ , and  $N$  are material constants. The quasi-static experimental data on high-purity  $\alpha$  titanium plate given in Table 1 and Table 2 were used to determine the coefficients (given in Table 3) of this criterion.

Table 1: Compressive yield data for high-purity  $\alpha$ -titanium used to identify Hill [12] parameter values.

Direction	$x$	$y$	$z$
Yield Strength (MPa)	142.7	208.5	246.8

Table 2: Tensile yield data for high-purity  $\alpha$ -titanium used to identify Hill’s [12] coefficients.

Direction	$x$	$45^\circ$	$y$	$z$
Yield Strength (MPa)	127.1	148.5	200.8	255.1

In Figure 33 are shown the theoretical yield loci according to Hill [12] along with the yield loci predicted by the anisotropic model developed as part of this research, and data on high-purity  $\alpha$ -titanium. Note that Hill’s [12] criterion cannot capture the observed behavior while the proposed model describes very well the pronounced strength differential effects displayed by the material.

### 3.3 Modeling anisotropic hardening during monotonic deformation of $\alpha$ -titanium

From the experimental data (see Figure 32, it appears that there is distortion of the shape of the yield surface of  $\alpha$ -titanium even for the simplest monotonic loading paths. This anisotropic hardening, which is due to evolving texture, cannot be described with existing isotropic or kinematic hardening laws. Recently, [31] proposed a method for accounting for texture evolution. This method allows for the variation of the anisotropy coefficients with accumulated plastic deformation, i.e. the linear transformation operator  $\mathbf{L}$  is no longer constant. However, obtaining analytic expressions for the evolution laws of all the  $L_{ij}$  components would be a difficult task. An alternate method is thus proposed. Specifically, using experimental yield stresses and numerical test results, the coefficients of the anisotropy tensor  $\mathbf{L}$  involved in the anisotropic yield criterion (9) are determined for a finite set of values of the equivalent plastic strain,  $\tilde{\varepsilon}$ . Next are calculated, the effective stress defined according to the proposed criterion and  $Y^j = Y(\boldsymbol{\sigma}^j, \tilde{\varepsilon}^j)$ , where  $Y$  defines the effective stress-effective plastic strain relationship in a given direction (e.g., the rolling direction). Further, an interpolation procedure is used to obtain the yield surfaces corresponding to any given level of accumulated strain. Indeed, note that the effective stress according to the proposed criterion can be written as

$$\tilde{\sigma} = A_1 \left[ (J_2)^{3/2} - cJ_3 \right]^{1/3} \quad (17)$$

where  $A_1$  is a constant defined such as to assure that  $\tilde{\sigma}$  reduces to the tensile yield stress in the rolling direction. Hence,

Table 3: Hill's [12] coefficients for high-purity  $\alpha$ -titanium.

Hill's (1948) Coefficients	$F$	$G$	$H$
Value	2.34E-05	-7.598E-06	3.15E-05

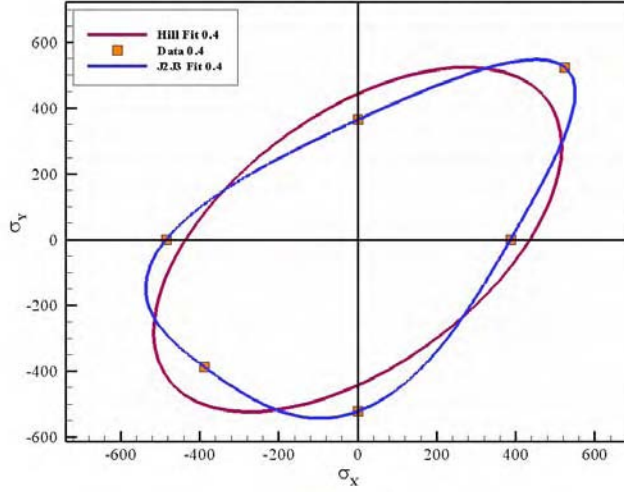


Figure 33: Theoretical yield loci according with Hill (1948) criterion and the proposed criterion 9 in comparison with experimental flow stresses (symbols) on high-purity  $\alpha$ -titanium.

$$A_1 = \left[ \frac{1}{3} (a_2^2 + a_3^2 + a_2 a_3)^{3/2} - \frac{c}{27} a_2 a_3 (a_2 + a_3) \right]^{-1/3} \quad (18)$$

For an arbitrary value of the accumulated plastic strain  $\tilde{\epsilon}^j \leq \tilde{\epsilon} \leq \tilde{\epsilon}^{j+1}$ , the anisotropic yield surface is:

$$\tilde{\sigma}_{current}(\boldsymbol{\sigma}, \tilde{\epsilon}) = Y_{current}(\boldsymbol{\sigma}, \tilde{\epsilon})$$

where

$$\tilde{\sigma}(\boldsymbol{\sigma}, \tilde{\epsilon})_{current} = \xi \tilde{\sigma}^j + (1 - \xi) \tilde{\sigma}^{j+1}$$

and

$$Y(\boldsymbol{\sigma}, \tilde{\epsilon})_{current} = \xi Y^j + (1 - \xi) Y^{j+1}$$

the interpolation parameter  $\xi$ , being defined as:

$$\xi = \frac{\tilde{\epsilon}^{j+1} - \tilde{\epsilon}}{\tilde{\epsilon}^{j+1} - \tilde{\epsilon}^j}$$

To simulate the response of high-purity  $\alpha$ -titanium, we will use the orthotropic criterion given by (4) and associated flow rule with hardening as described by the interpolative procedure described above.

### 3.4 Integration algorithm of the proposed model, finite-element implementation, and simulation of the response of high-purity $\alpha$ titanium in uniaxial tension/compression

The developed orthotropic yield criterion (see (9)) in conjunction with the anisotropic hardening law presented in the previous section and associated flow rule was implemented into EPIC2003, the 2003 version of the explicit finite element code EPIC (Elastic Plastic Impact Calculations). EPIC code has been developed by Dr. Gordon Johnson under the primary sponsorship of the U.S. Air Force and U.S. Army. The first documented version proposed in 1977 was 2D only but has later evolved into a one, two or three-dimensional version with many additions and enhancements. All simulations were carried out on a PC platform using Compaq Visual Fortran Professional Edition 6.6.a. The code was compiled such that all real variables were double precision.

Given the current stress state, the current strain rate, and the current time step, a user's subroutine was developed in order to update the stress state. The integration algorithm solves for the updated stresses by enforcing the Kuhn-Tucker and consistency conditions. As already mentioned, an associated flow rule was assumed such that the stress potential  $G$  is the same as the yield function  $f^o$  (see (9))

$$\Delta \boldsymbol{\varepsilon}_p = \Delta \lambda \frac{\partial f^o}{\partial \boldsymbol{\sigma}} \quad (19)$$

where  $\Delta \boldsymbol{\varepsilon}_p$  is the plastic strain increment,  $\Delta \lambda$  is the plastic scalar multiplier,  $f^o$  is the proposed anisotropic yield function, and  $\boldsymbol{\sigma}$  is the Cauchy stress tensor. Within the stress update subroutine, an updated trial stress is computed assuming elastic response, i.e.  $d\boldsymbol{\sigma} = \mathbf{C}^e d\boldsymbol{\varepsilon}$ , where  $\mathbf{C}^e$  is the fourth-order elastic compliance tensor. The updated trial stress is computed as  $\boldsymbol{\sigma}_{updated} = \boldsymbol{\sigma}_{current} + d\boldsymbol{\sigma}$ . Next, an equivalent stress ( $\tilde{\boldsymbol{\sigma}}$ ) is computed according to the proposed anisotropic yield criterion and compared to the current value of the hardening function ( $Y_S$ ). If  $\tilde{\boldsymbol{\sigma}} \leq Y_S$  the current stress state is elastic, the trial stress coincides with the actual stress. If  $\tilde{\boldsymbol{\sigma}} > Y_S$ , then an implicit iterative scheme is used to return the stress state to the yield surface. The initial guess for this iterative process is  $\tilde{\boldsymbol{\sigma}}$ . The total accumulated plastic strain ( $\bar{\boldsymbol{\varepsilon}}$ ) is taken as the hardening parameter, the yield criterion being

$$f(\boldsymbol{\sigma}, \bar{\boldsymbol{\varepsilon}}) = \tilde{\boldsymbol{\sigma}}(\boldsymbol{\sigma}, \bar{\boldsymbol{\varepsilon}}) - Y_s(\bar{\boldsymbol{\varepsilon}}) \quad (20)$$

In the following  $j$  is used as the global counter, i.e.  $j$  is the current state, and  $j + 1$  is the fully updated state and  $n$  is used as a local iteration counter, i.e.  $n$  is the current iteration and  $n + 1$  is the updated iteration count. Then, the total increment of stress for a given iteration step is

$$\Delta \boldsymbol{\sigma}_{n+1}^{j+1} = \Delta \boldsymbol{\sigma}_n^{j+1} + \delta \boldsymbol{\sigma}_{n+1}^{j+1} \quad (21)$$

where  $\Delta$  indicates an increment over the entire time step and  $\delta$  indicates an increment for each iteration. The plastic correction to the stress is

$$\delta \boldsymbol{\sigma}_{n+1}^{j+1} = \delta \lambda_{n+1}^{j+1} \mathbf{C} : \left. \frac{\partial \tilde{\boldsymbol{\sigma}}}{\partial \boldsymbol{\sigma}} \right|_{n+1}^{j+1} \quad (22)$$

The derivatives of the equivalent stress are found by taking only the first term of a Taylor series expansion about the current state

$$\left. \frac{\partial \tilde{\sigma}}{\partial \boldsymbol{\sigma}} \right|_{n+1}^{j+1} \approx \left. \frac{\partial \tilde{\sigma}}{\partial \boldsymbol{\sigma}} \right|_n^{j+1} + \left. \frac{\partial^2 \tilde{\sigma}}{\partial \boldsymbol{\sigma}^2} \right|_n^{j+1} \delta \boldsymbol{\sigma} + \left. \frac{\partial^2 \tilde{\sigma}}{\partial \boldsymbol{\sigma}} \partial \bar{\varepsilon} \right|_n^{j+1} \delta \lambda \quad (23)$$

Keeping only the first term in (23), Equation (22) becomes

$$\delta \boldsymbol{\sigma}_{n+1}^{j+1} \approx \delta \lambda_{n+1}^{j+1} \mathbf{C} : \left. \frac{\partial \tilde{\sigma}}{\partial \boldsymbol{\sigma}} \right|_n^{j+1} \quad (24)$$

Solving for the increment for a given iteration gives

$$\delta \boldsymbol{\sigma}_{n+1}^{j+1} = -\mathbf{C}^{-1} : \delta \lambda_{n+1}^{j+1} \left. \frac{\partial \tilde{\sigma}}{\partial \boldsymbol{\sigma}} \right|_n^{j+1} \quad (25)$$

A Taylor series expansion of the yield criterion is used to obtain an approximation of the increment of the effective plastic strain

$$f(\boldsymbol{\sigma}_{n+1}^{j+1}, \bar{\varepsilon}_{n+1}^{j+1}) \approx f(\boldsymbol{\sigma}_n^{j+1}, \bar{\varepsilon}_n^{j+1}) + \left. \frac{\partial f}{\partial \bar{\varepsilon}} \right|_n^{j+1} \delta \lambda_{n+1}^{j+1} = 0 \quad (26)$$

Evaluating derivatives at the previous step, equations (25) and (26) can be used to give

$$\delta \lambda_{n+1}^{j+1} = \frac{f(\boldsymbol{\sigma}_n^{j+1}, \bar{\varepsilon}_n^{j+1})}{\left. \frac{\partial \tilde{\sigma}}{\partial \boldsymbol{\sigma}} \mathbf{C}^{-1} \frac{\partial \tilde{\sigma}}{\partial \boldsymbol{\sigma}} + \frac{\partial Y_S}{\partial \bar{\varepsilon}} - \frac{\partial \tilde{\sigma}}{\partial \bar{\varepsilon}} \right|_n^{j+1}} \quad (27)$$

This can now be used in equation (25) to find  $\delta \boldsymbol{\sigma}_{n+1}^{j+1}$  and finally, the total stress increment is found from equation (21). This new stress is then evaluated to see if it has converged within a specified tolerance. If not, this is used as the starting stress for the next iteration. When the stress has converged, the global stress tensor is updated and returned to the main program. Derivatives of the yield function with respect to the stress are used in integrating the increments of plastic strain in the FE implementation. The general form can be written as

$$\frac{\partial F}{\partial \boldsymbol{\sigma}} = \frac{\partial F}{\partial J_2^o} \frac{\partial J_2^o}{\partial \boldsymbol{\Sigma}} \frac{\partial \boldsymbol{\Sigma}}{\partial \boldsymbol{\sigma}} + \frac{\partial F}{\partial J_3^o} \frac{\partial J_3^o}{\partial \boldsymbol{\Sigma}} \frac{\partial \boldsymbol{\Sigma}}{\partial \boldsymbol{\sigma}}$$

or

$$\frac{\partial F}{\partial \sigma_{ij}} = \frac{\partial F}{\partial J_2^o} \frac{\partial J_2^o}{\partial \Sigma_{kl}} \frac{\partial \Sigma_{kl}}{\partial \sigma_{ij}} + \frac{\partial F}{\partial J_3^o} \frac{\partial J_3^o}{\partial \Sigma_{kl}} \frac{\partial \Sigma_{kl}}{\partial \sigma_{ij}} \quad (28)$$

where

$$\frac{\partial F}{\partial J_2^o} = \frac{\Theta (J_2^o)^{1/2}}{2 ((J_2^o)^{3/2} - c J_3^o)^{2/3}}$$

$$\frac{\partial F}{\partial J_3^o} = -\frac{\Theta c}{3((J_2^o)^{3/2} - c J_3^o)^{2/3}}$$

The derivatives with respect to  $\Sigma$  are

$$\begin{aligned} \frac{\partial J_2^o}{\partial \Sigma_{11}} &= \Sigma_{11} & \frac{\partial J_2^o}{\partial \Sigma_{22}} &= \Sigma_{22} & \frac{\partial J_2^o}{\partial \Sigma_{33}} &= \Sigma_{33} \\ \frac{\partial J_2^o}{\partial \Sigma_{12}} &= 2\Sigma_{12} & \frac{\partial J_2^o}{\partial \Sigma_{13}} &= 2\Sigma_{13} & \frac{\partial J_3^o}{\partial \Sigma_{23}} &= 2\Sigma_{23} \end{aligned}$$

$$\begin{aligned} \frac{\partial \Sigma_{11}}{\partial \sigma_x} &= \frac{1}{3}(a_2 + a_3) & \frac{\partial \Sigma_{22}}{\partial \sigma_x} &= -\frac{1}{3}a_3 & \frac{\partial \Sigma_{33}}{\partial \sigma_x} &= -\frac{1}{3}a_2 \\ \frac{\partial \Sigma_{11}}{\partial \sigma_y} &= -\frac{1}{3}a_3 & \frac{\partial \Sigma_{22}}{\partial \sigma_y} &= \frac{1}{3}(a_1 + a_3) & \frac{\partial \Sigma_{33}}{\partial \sigma_y} &= -\frac{1}{3}a_1 \\ \frac{\partial \Sigma_{11}}{\partial \sigma_z} &= -\frac{1}{3}a_2 & \frac{\partial \Sigma_{22}}{\partial \sigma_z} &= -\frac{1}{3}a_1 & \frac{\partial \Sigma_{33}}{\partial \sigma_z} &= \frac{1}{3}(a_1 + a_2) \\ \frac{\partial \Sigma_{12}}{\partial \tau_{xy}} &= a_4 & \frac{\partial \Sigma_{13}}{\partial \sigma_{xz}} &= a_5 & \frac{\partial \Sigma_{23}}{\partial \sigma_{yz}} &= a_6 \end{aligned}$$

All other derivatives are equal to zero.

The FE implementation uses the methodology for describing the evolution of the yield surface due to texture changes presented in the previous section. A sufficient number of points was used to ensure that the hardening curve was recreated with enough accuracy. For each of these strain levels, ranging from 0 to 50%, the corresponding yield surfaces according to Equation (9) were determined. The anisotropy coefficients shown in Table 4 were calculated following the identification procedure described in Section 3.2.

For the material investigated, the iso-strain contours of the theoretical biaxial yield surfaces compared to data are shown in Figure 34 A. The data used to identify the model parameters are represented in Figure 34 B by symbols. Recall that to obtain the tensile data for strains larger than 20% strain required an extrapolation because the material began to localize beyond this strain level. Note that the model reproduces the data quite well with the largest difference between theoretical and experimental values being for the biaxial stress state. Table 4 gives the uniaxial stresses in the RD and anisotropy coefficient values determined at each strain level for our material.

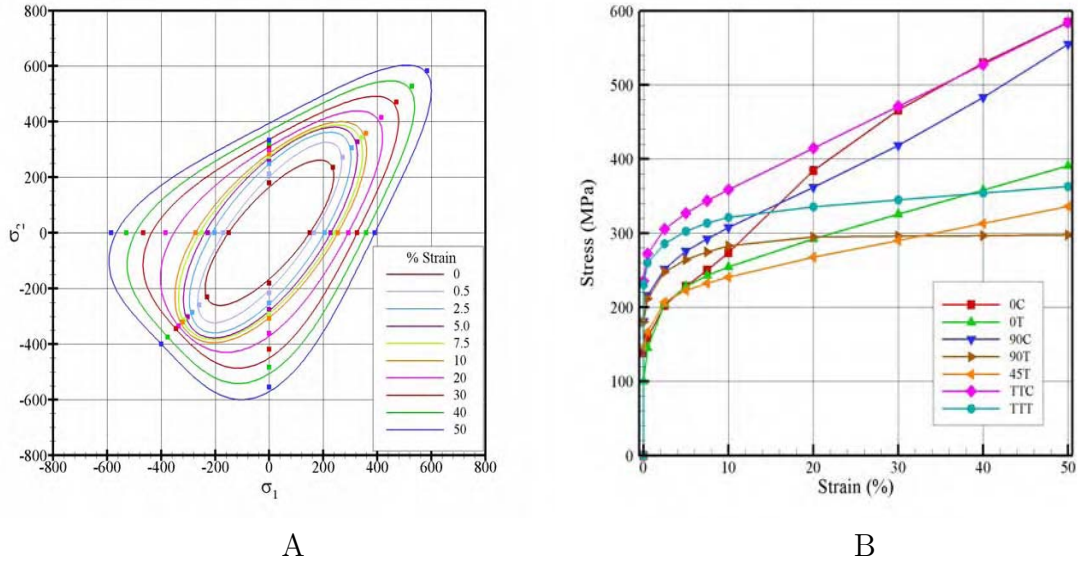


Figure 34: A) Theoretical yield surfaces for fixed levels of accumulated plastic strain; B) Data used in identifying the theoretical yield surfaces.

### 3.5 Application of the proposed model to $\alpha$ -titanium

The proposed model was used for simulation of the response of the  $\alpha$ -titanium material investigated for uniaxial loading condition. The model was then validated by simulating the four point bend tests described in the section 3.6. A comparison was made in a qualitative way by juxtaposing contours of the experimental data against the results from the simulation for all four loading scenarios. Comparison of the experimental cross sections of the beams and simulated ones using the model and an isotropic material with a von Mises yield surface were also performed. A quantitative comparison was done by comparing axial strain versus height at the centerline of each beam specimen.

Table 4: Anisotropy coefficients for discrete strain levels

Strain	Yield	a1	a2	a3	a4	a5	a6	c
0.0000	208	0.5454	0.5010	1.0900	0.7246	-0.8675	-0.8675	-0.2168
0.0250	245	0.5231	0.4745	0.9034	0.7309	0.7202	0.7202	-0.2198
0.0500	261	0.6694	0.5585	1.1030	0.9138	0.9381	0.9381	-0.2291
0.0750	273	0.6960	0.5969	1.1270	0.9838	0.9716	0.9716	-0.2607
0.1000	284	0.5356	0.4768	0.8603	0.7761	0.7714	0.7714	-0.2754
0.2000	317	0.0610	0.0576	0.0869	0.0870	0.0794	0.0794	-0.5908
0.4000	370	0.0632	0.0620	0.0788	0.0816	0.0801	0.0801	-1.0330
0.5000	389	0.9547	0.9570	1.2140	1.1810	1.1760	1.1760	-1.1480

Note: Yield Strength in MPa

For uniaxial loading conditions, the simulations involved a single element with eight nodes with a single integration point (see Figure 35). The cell was stretched uniaxially and the obtained stress versus strain results were compared to the appropriate experimental data. For each simulation, four nodes on one face of the element were restrained and the four nodes on the opposite face were given a constant velocity in either the tensile or compressive direction.

The simulated normal stresses in the appropriate loading direction versus the effective strain

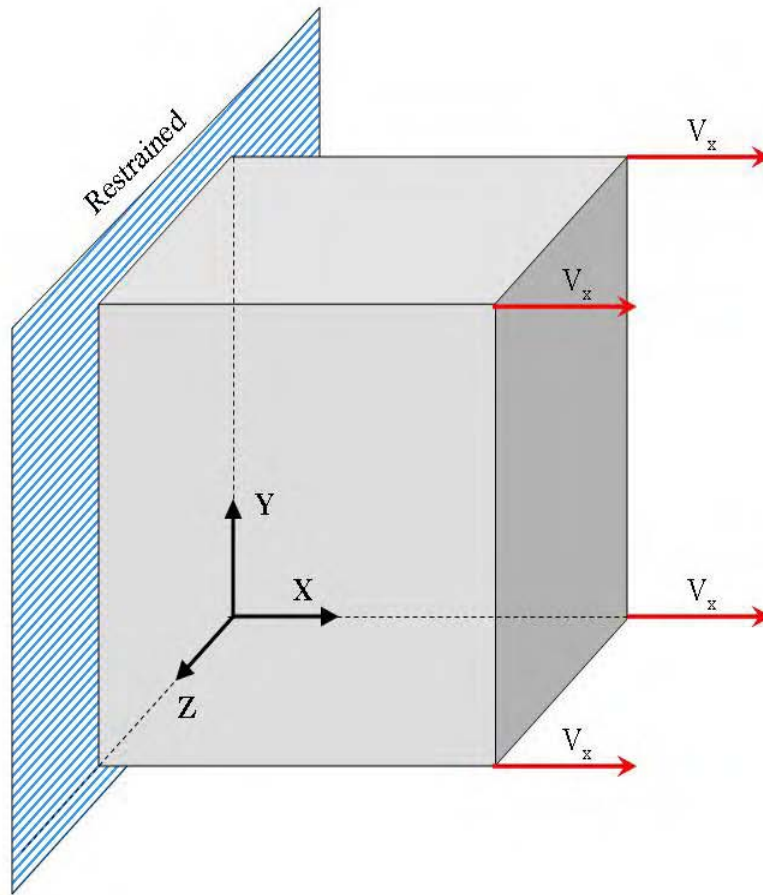
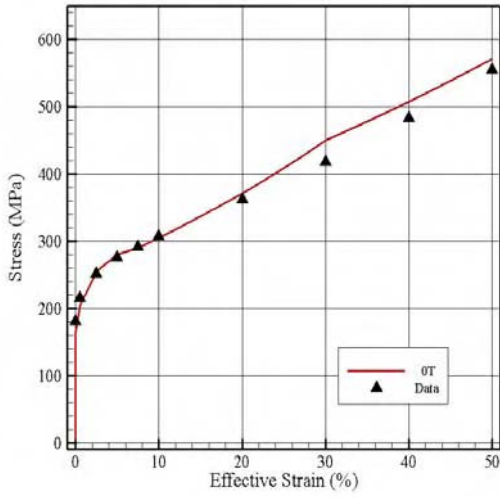
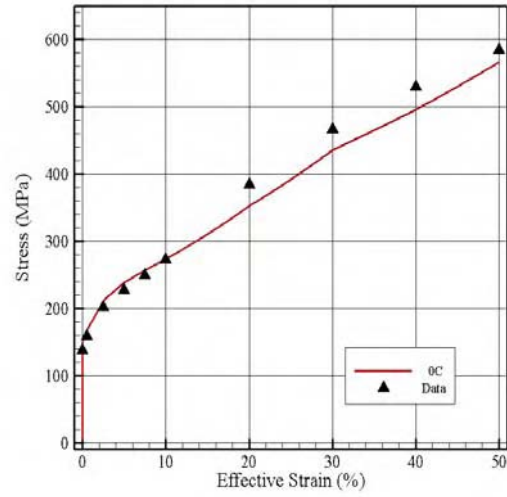


Figure 35: Single cell computational configuration

are compared to the corresponding experimental data (see Figures 36 to 38). Note that the model accurately reproduces the data for each loading condition. The largest discrepancy occurs for the  $90^\circ$  tensile data, which is due to the slight discrepancy between experimental and predicted flow stresses in this direction that was noted previously.

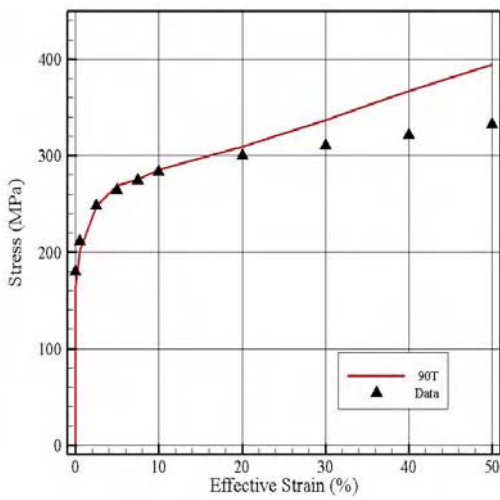


A

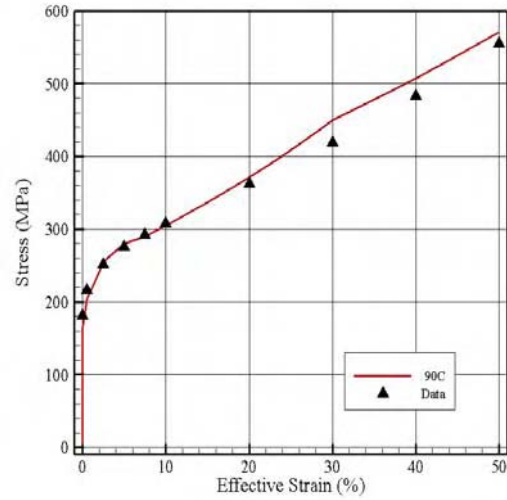


B

Figure 36: Comparison between finite element simulation results using the proposed model and experimental data corresponding to uniaxial loading in the rolling direction: A) tension; B) compression.



A



B

Figure 37: Comparison between finite element simulation results using the proposed model and experimental data corresponding to uniaxial loading in the transverse direction: A) tension B) compression.

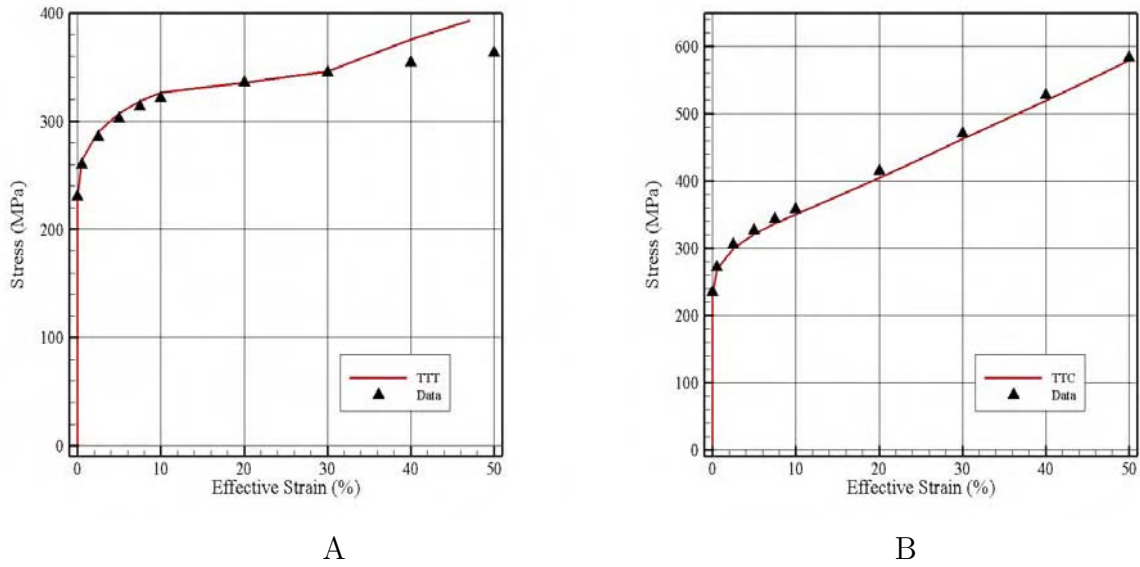


Figure 38: Comparison between finite element simulation results using the proposed model and experimental data corresponding to uniaxial loading in the through-thickness direction : A) tension B) compression.

### 3.6 Model validation results

Finite-element simulations of beam bending tests were conducted. The simulated final cross sections for the four configurations are shown in Figure 39. As expected, when the hard direction (TT) is perpendicular to the loading direction (Cases 1 and 3) the cross section remains nearly square. Case 2 and Case 4 are similar to each other with more lateral strain in Case 4. This is consistent with the material being harder in the TD than in the RD as shown in the uniaxial tests (see Figure 40 which show that for strain levels below 15%, the material is stronger in the TD direction for both tensile and compressive loading). For comparison purposes, FE simulations using the isotropic von Mises yield criterion in conjunction with an isotropic hardening law based on the RD tension data were conducted and compared to the results obtained using the anisotropic model (see Figure 41). Note that in Case 1 and Case 3, the hard direction (TT) is the width direction and the isotropic simulation shows more deformation than it is obtained using the anisotropic model. For Case 2 and Case 4 there is less deformation in the height of the beam and the width shows deformation similar to the isotropic simulation. Again this is because for these loading scenarios, the softer direction is aligned with the width. For each loading scenario, comparisons between FE axial strain contours obtained with the proposed anisotropic model and experimental axial strain contours obtained by digital image correlation are presented. The beam orientation for Case 1 loading is shown in Figure 42 for reference while Figure 43 shows the comparison of the respective strain profiles. A very

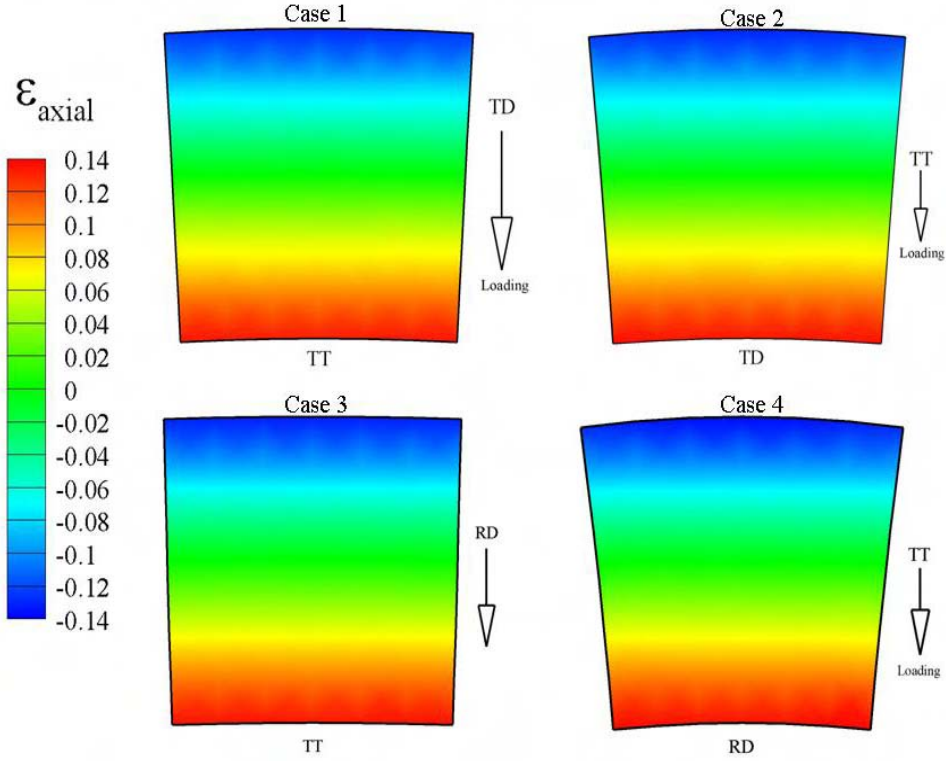


Figure 39: Simulated final cross sections for the four beam configurations

good agreement is obtained. Note that the data from the experiment does not cover the entire profile area due to the DIC [[42, 43]] techniques used.

A more qualitative comparison is presented in Figure 44, which shows a plot of the axial strain versus the height of the beam at the center of the beam. A very good agreement between the experiment and simulation is observed. In particular, the upward shift of the neutral axis of the beam is very well captured. To provide a final validation of the model, the beams were sectioned at the midpoint and a photograph of the cross section was compared to the simulation results. The comparison between theory and data for Case 1 is shown in Figure 45. Note that there is very little deformation perpendicular to the loading direction because this is the harder to deform direction.

The beam orientation for Case 2 is shown in Figure 46 for reference, while Figure 47 shows the comparison of the respective strain profiles. Again, very good agreement is shown between experimental data and the simulation results obtained using the proposed model. Note that the model predicts somewhat less strain through the thickness in the loading direction.

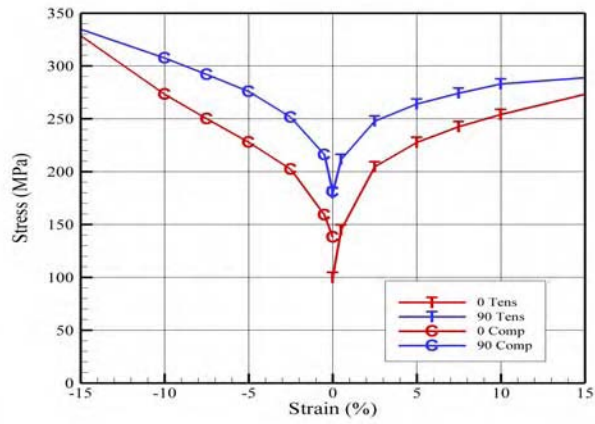


Figure 40: Comparison between stress-strain response in tension and compression and experimental data for RD and TD directions, respectively.

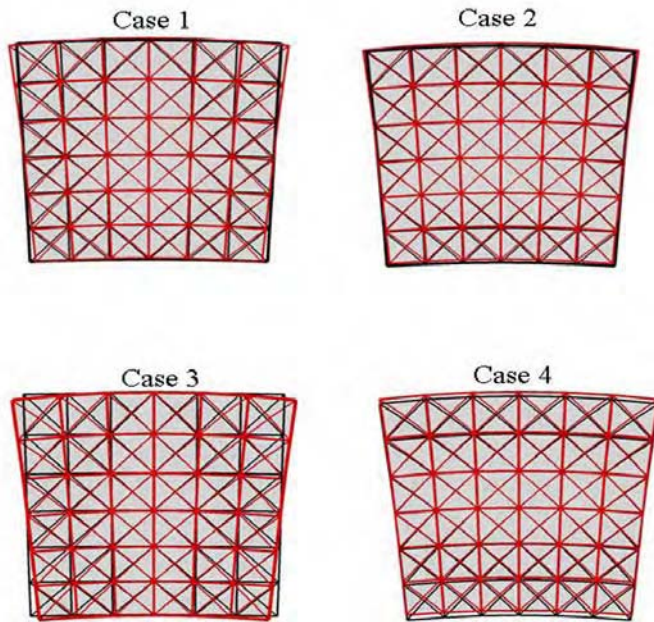


Figure 41: Comparison of the final cross sections of the beam specimens as predicted by the proposed model and by an isotropic von Mises model (red mesh)

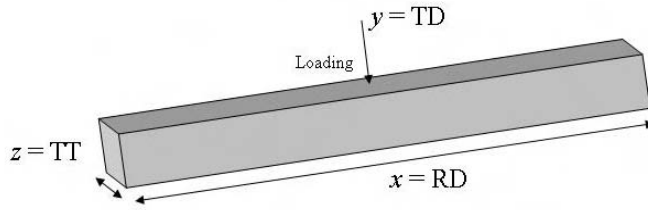


Figure 42: Case 1: Long axis in RD direction, loading in the TD direction.

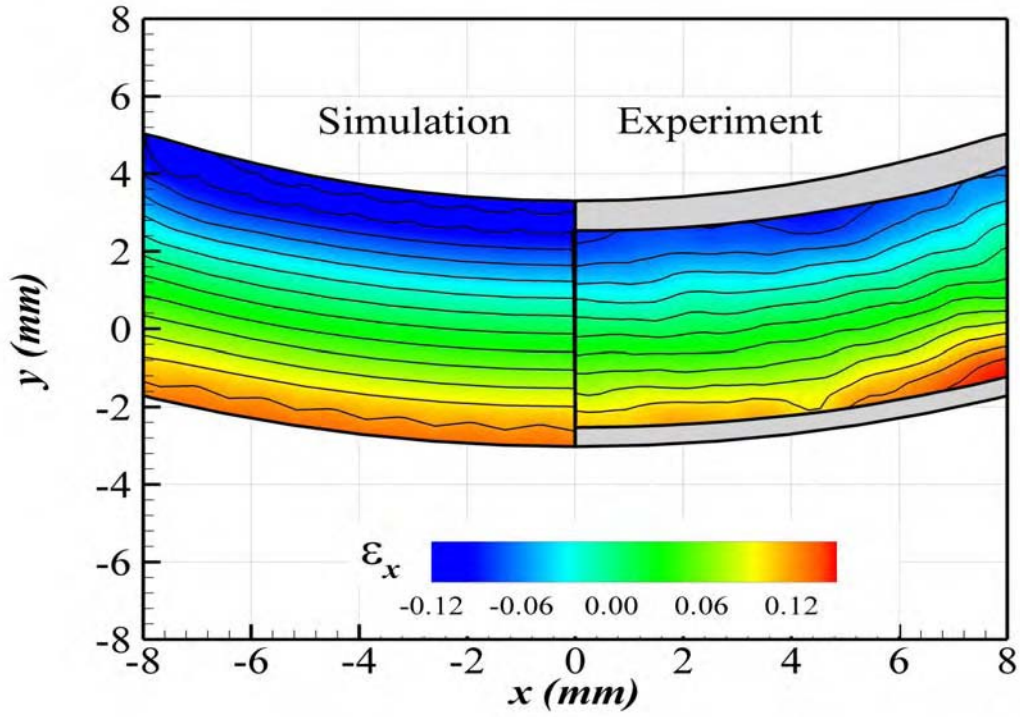


Figure 43: Case 1 loading: comparison of FE axial strain contours ( $\epsilon_x$ ) obtained with the proposed model against experimental data:  $x = \text{RD}$ ,  $y = \text{TD}$ .

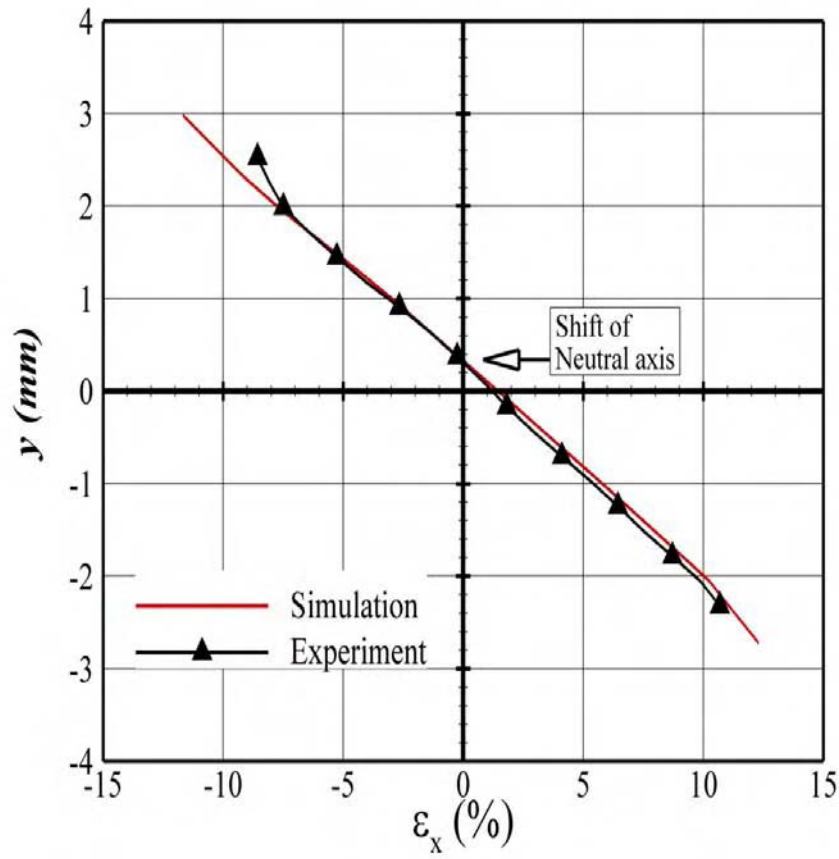


Figure 44: Plate 1, Case 1: Axial strains ( $\epsilon_x$ ) versus height at centerline:  $x=RD$ ,  $y=TD$ .

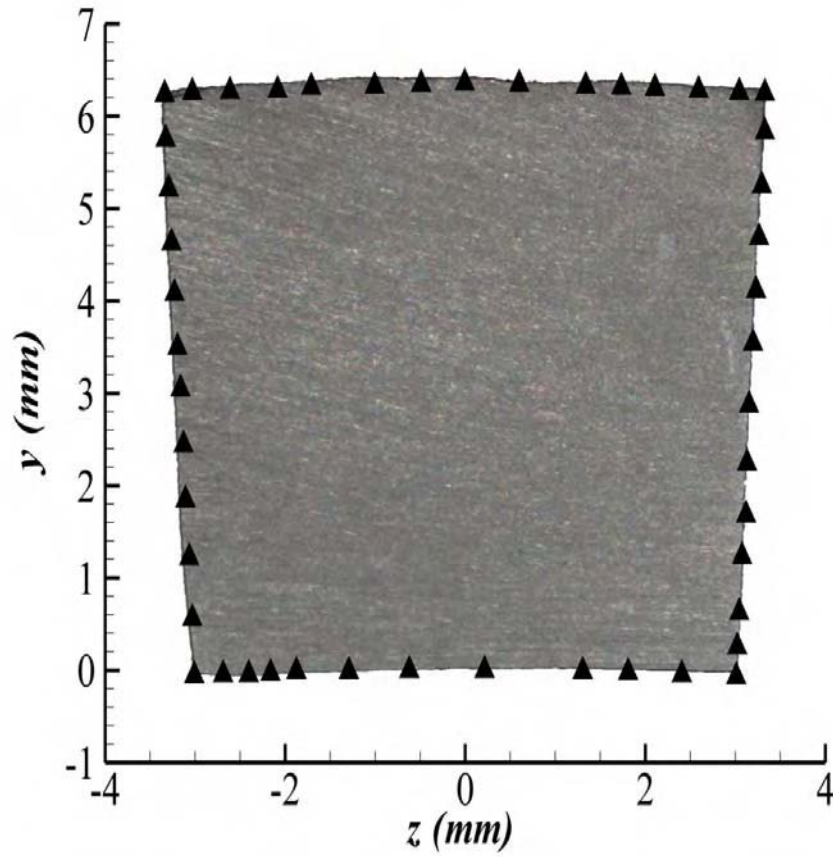


Figure 45: Case 1: Comparison of the photographed experimental cross sections and FE simulation using the proposed model(symbols):  $y=TD$ ,  $z=TT$ .

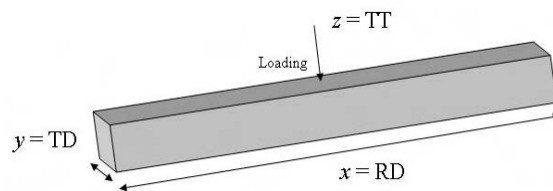


Figure 46: Case 2 loading: Long axis in the RD, loading in TT

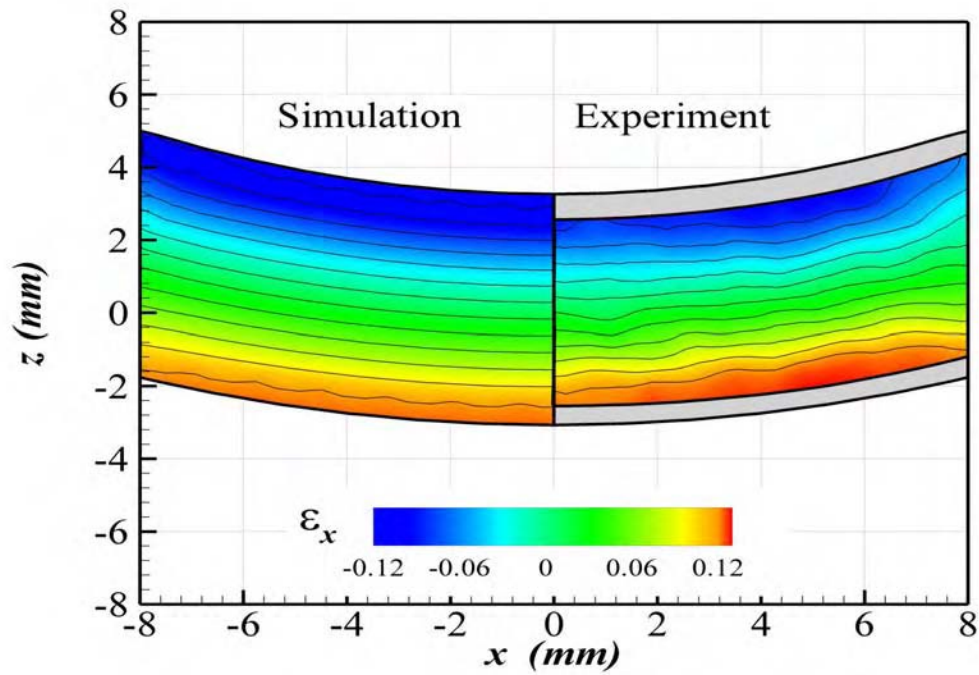


Figure 47: Case 2: Comparison of the photographed experimental cross sections and FE simulation using the proposed model(symbols):  $x=RD$ ,  $z=TT$

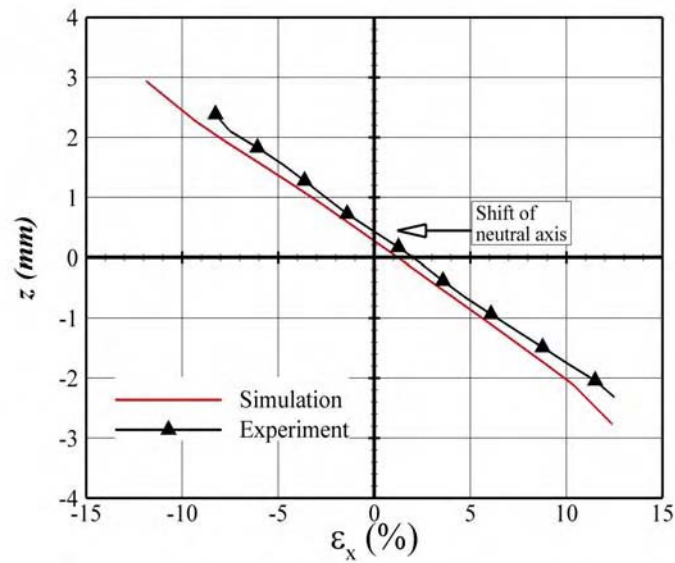


Figure 48: Case 2: Axial strains ( $\epsilon_x$ ) versus height at centerline:  $x=RD$ ,  $z=TT$

A plot of the axial strain versus the height of the beam at the center of the beam is shown in Figure 48. Note the very good agreement between the experiment and simulation and the clear upward shift of the neutral axis of the beam due to the tension-compression asymmetry of the material, which is very well described by the model.

The comparison of final cross sections of the beam in Case 2 loading is shown in Figure 49. Again, there is a very good agreement. Note that the model predicts with accuracy that there is more deformation perpendicular to the loading direction because in Case 2, the loading direction is the softer transverse direction. The beam orientation for Case 3 is shown in Figure

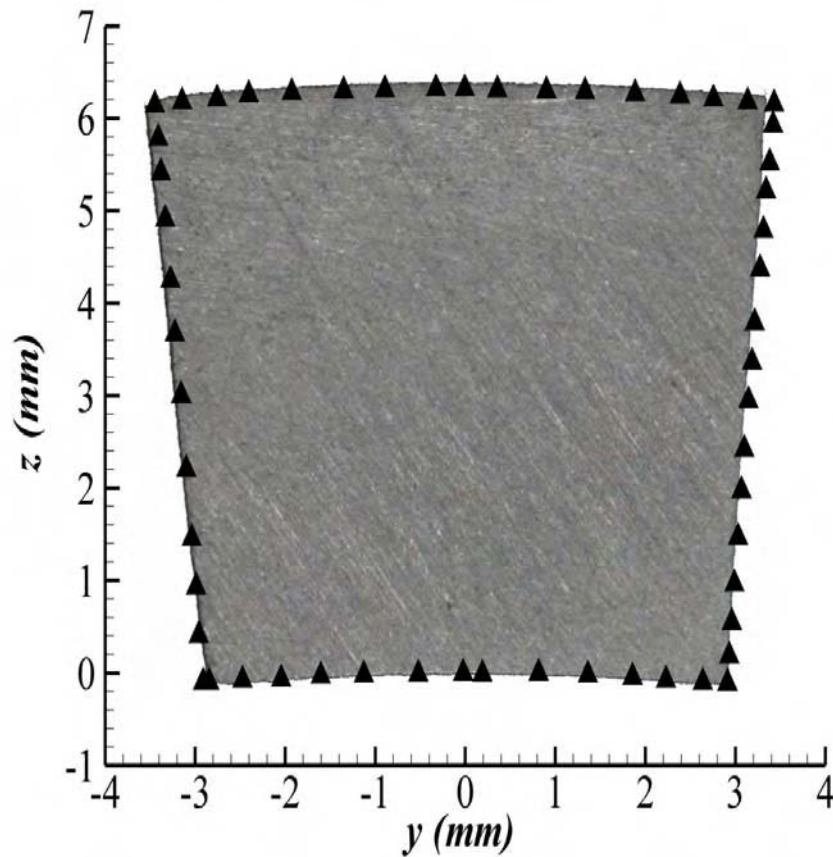


Figure 49: Case 2: Comparison of the photographed experimental cross sections and FE simulation using the proposed model (symbols):  $y=TD$ ,  $z=TT$

50 for reference while Figure 51 shows the comparison between experimental and simulated strain profiles. Again, very good agreement is obtained.

A plot of the axial strain versus the height of the beam at the center of the beam is shown in Figure 52. Note the very good agreement between the experiments and simulation results.

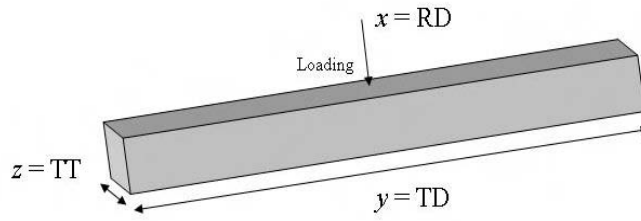


Figure 50: Case 3: Long axis in the TD direction, loading in the RD direction

The upward shift of the neutral axis is very well described by the model. The comparison of the photographed and simulated final cross sections is shown in Figure 53. Note the excellent agreement.

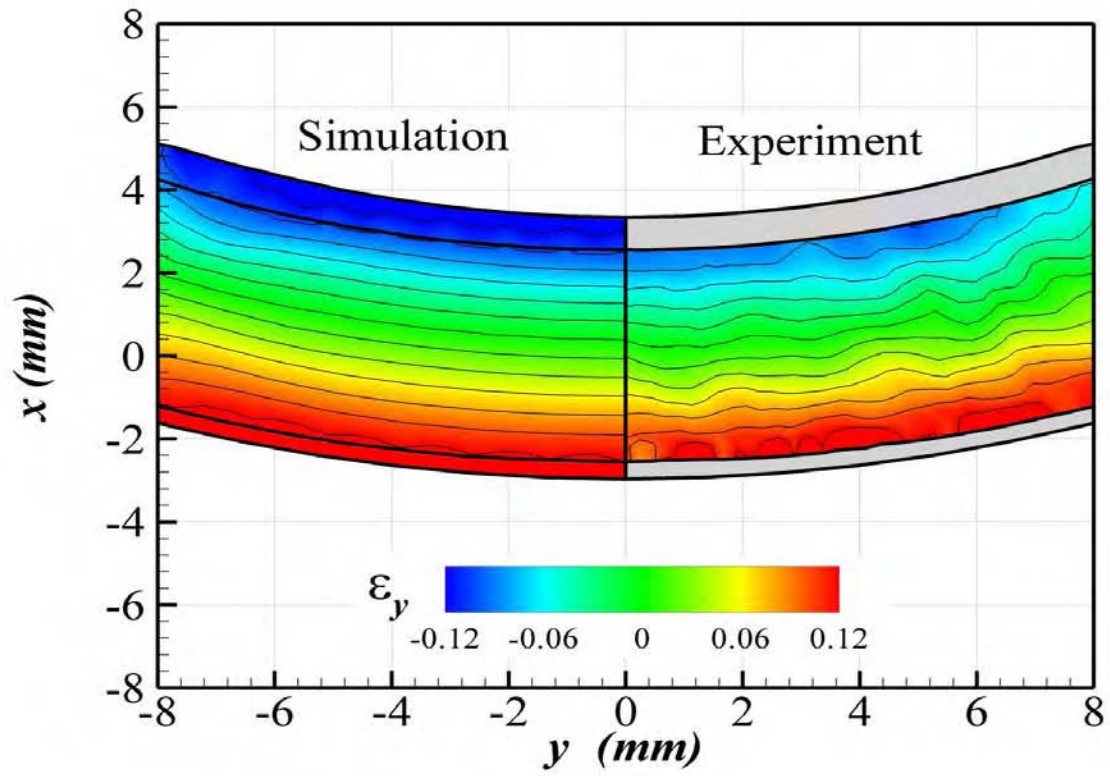


Figure 51: Case 3: Comparison of the FE axial strain contours ( $\epsilon_y$ ) obtained with the proposed model against experimental data:  $x=RD$ ,  $y=TD$

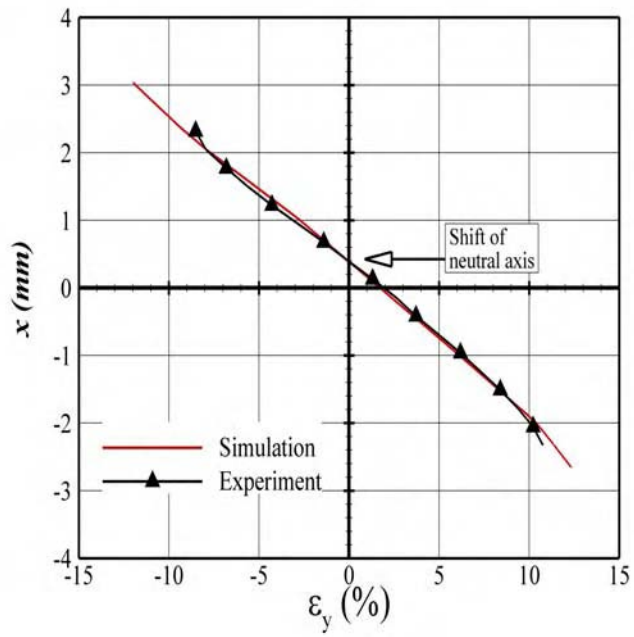


Figure 52: Case 3: Axial strains ( $\epsilon_y$ ) versus height at centerline:  $x=RD$ ,  $y=TD$

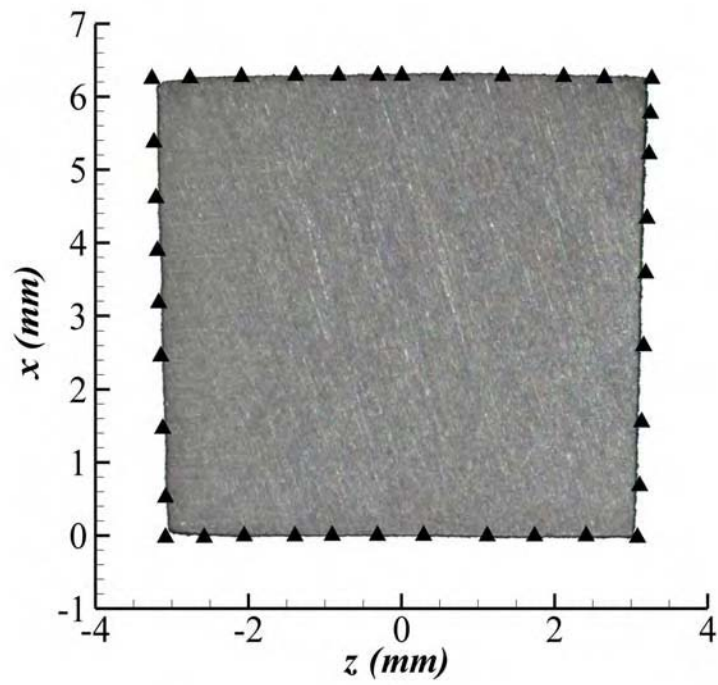


Figure 53: Case 3: Comparison of the photographed experimental cross sections and FE simulation using the proposed model(symbols):  $x$ =RD,  $z$ =TT

The beam orientation for Case 4 is shown in Figure 54 for reference while Figure 55 shows the comparison of the simulated and experimental axial strain contours for Case 4 . Again, very good agreement is shown.

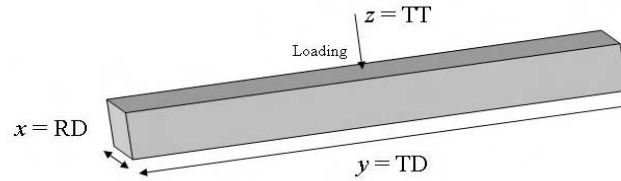


Figure 54: Case 4: Long axis in the TD direction, loading in the TT direction

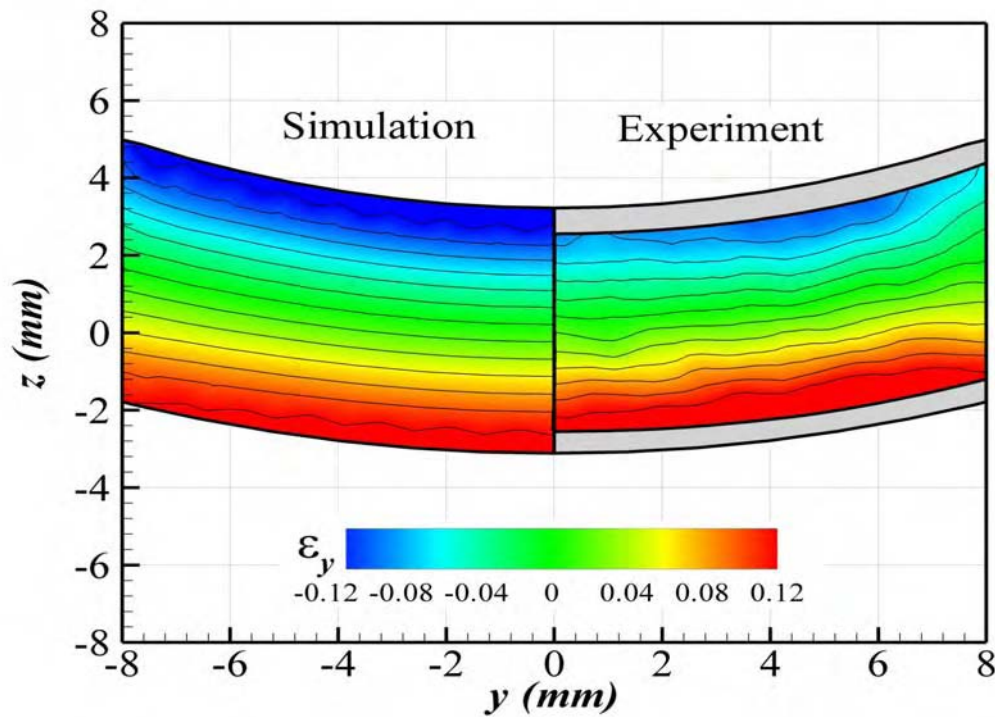


Figure 55: Case 4: Comparison of experimental and simulated axial strain contours ( $\epsilon_y$ ) :  $y = \text{TD}$ ,  $z = \text{TT}$

The axial strain at the center of the beam along the height of the beam is shown in Figure 56. Note the very good agreement between the experimental and simulation results, in particular the upward shift of the neutral axis of the beam, which is due to the tension-compression symmetry of the material. A very good agreement between experimental and simulated final cross sections for Case 4 is also obtained (see Figure 57).

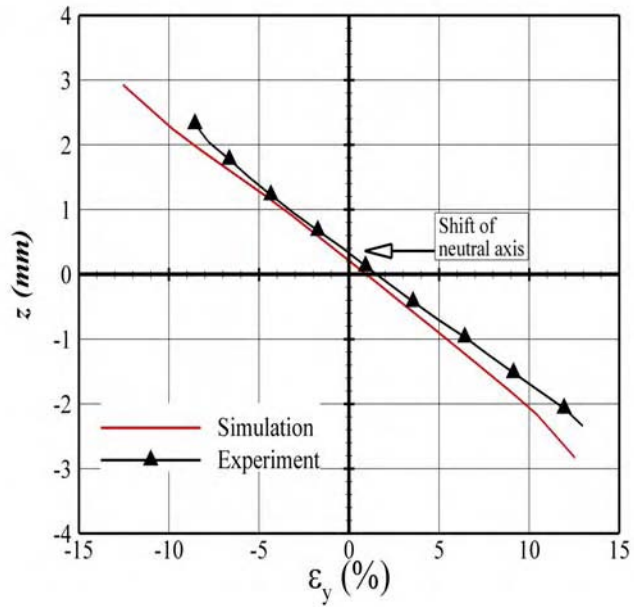


Figure 56: Case 4: Axial strains ( $\varepsilon_y$ ) versus height at centerline:  $y=TD$ ,  $z=TT$

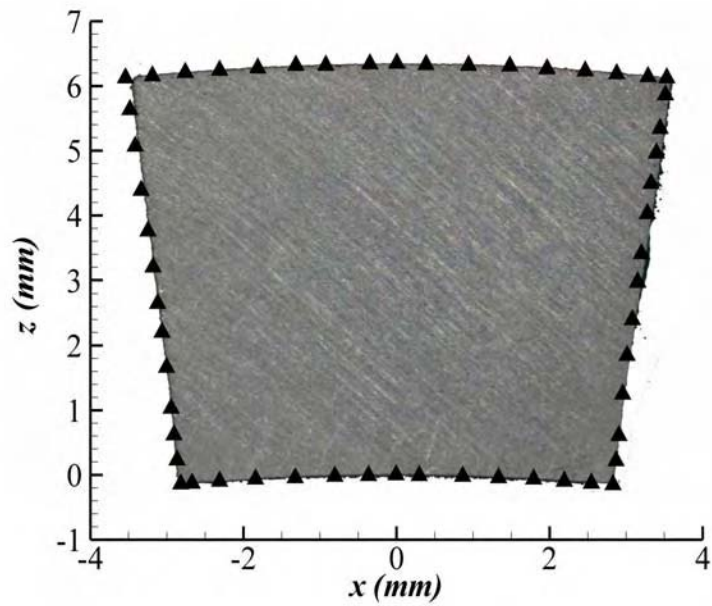


Figure 57: Plate 1, Case 4: Comparison of the photographed experimental and simulated (symbols) cross sections :  $x=RD$ ,  $z=TT$

## 4 Characterization of the high-strain rate behavior of high-purity $\alpha$ -titanium

High rate loading tests were carried out using a split Kolsky-Hopkinson pressure bar at Eglin Air Force Base, Florida. High rate compression specimens (Figures 58 A) ) were simple cylinders of 0.2 x 0.2 inches thus smaller than the specimens used for the quasi-static compression tests. High-rate tensile specimens were cylindrical dog bones as shown in Figure 58 (B) and were marked with an arrow indicating the top of the plate and therefore the through thickness direction. The plate thickness did not allow enough material to obtain high-rate through thickness tension specimens.

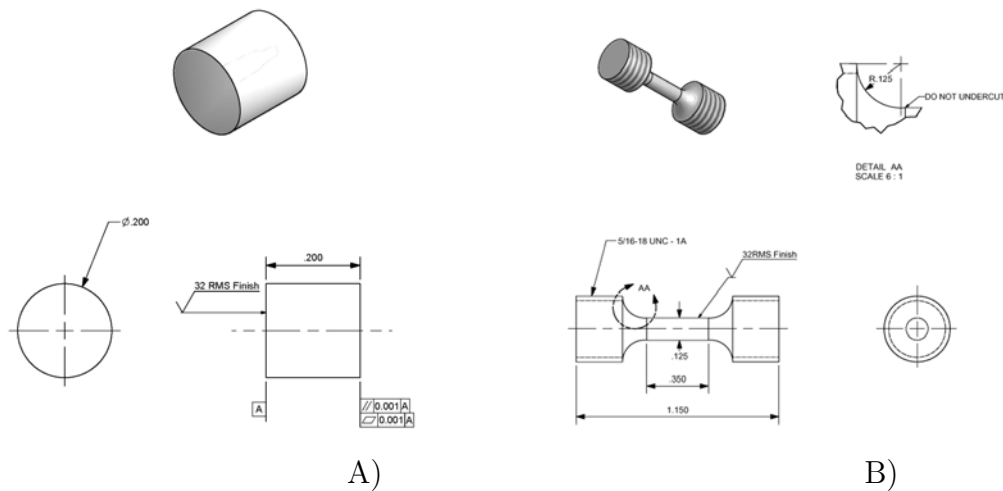


Figure 58: High rate test specimens: A) for compressive loading; B) for tensile loading.

All tensile tests were carried out to failure. A typical cross section of the failed specimen is shown in Figure 59. Note the cup-cone failure and the elliptical shape of the final cross-section, with the harder, through-thickness direction in the direction of the major axis of the specimen. Both compressive and tensile tests were carried out on specimens cut along the rolling, transverse, and through-thickness directions, respectively at nominal strain rates ranging from 400 to 600/s (see Fig. 60 and Tables 5 and 6 ). Table 7 gives the yield values for several levels of strain as well as the anisotropy ratio (defined as the ratio of highest to lowest yield at a given strain level) for both the high loading rate data and the quasi-static data. The test results show that the material response at high-strain rate is also orthotropic. The transverse direction stress-strain curve remains below the through-thickness stress-strain curve throughout, as in the quasi-static case. As in the case of quasi-static loading, the plate material is initially harder in the through-thickness direction but after 15% strain, the flow stress in the rolling direction is the largest.

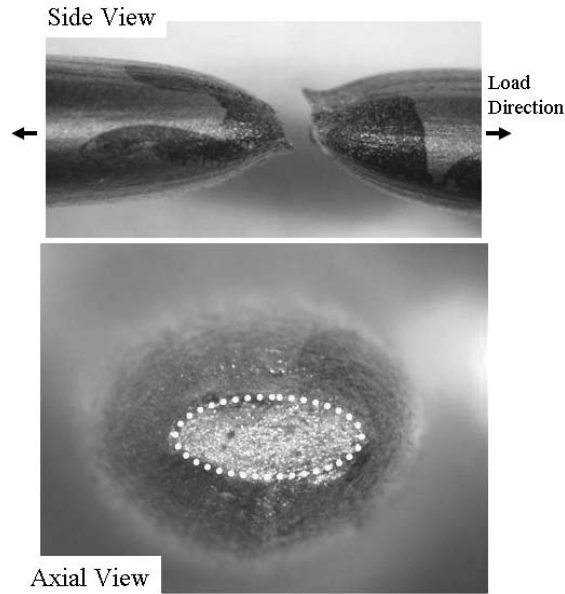


Figure 59: Post-test specimen with long axis along in-plane direction, subjected to high-strain rate tensile loading showing cup-cone fracture and elliptical final cross-section.

Table 5: Strain rates achieved in tensile Split-Hopkinson Bar (SHPB) tests

Test Number	1	2	3	4	5	6	7	8	9	10
Strain Rate ( $\text{sec}^{-1}$ )	522	517	643	665	652	627	662	653	555	543
Test Number	11	12	13	14	15	16	17	18	19	20
Strain Rate ( $\text{sec}^{-1}$ )	585	534	547	563	573	528	552	557	529	516
Test Number	21	22	23							
Strain Rate ( $\text{sec}^{-1}$ )	517	616	531							

Note: AVG = 567 and Standard Dev = 53

Table 6: Strain rates achieved for tensile SHPB tests

Test Number	1	2	3	4	5	6	7	8	9	10
Strain Rate ( $\text{sec}^{-1}$ )	419	429	318	369	396	466	457	408	417	403

Note: AVG = 407 and Standard Dev = 42

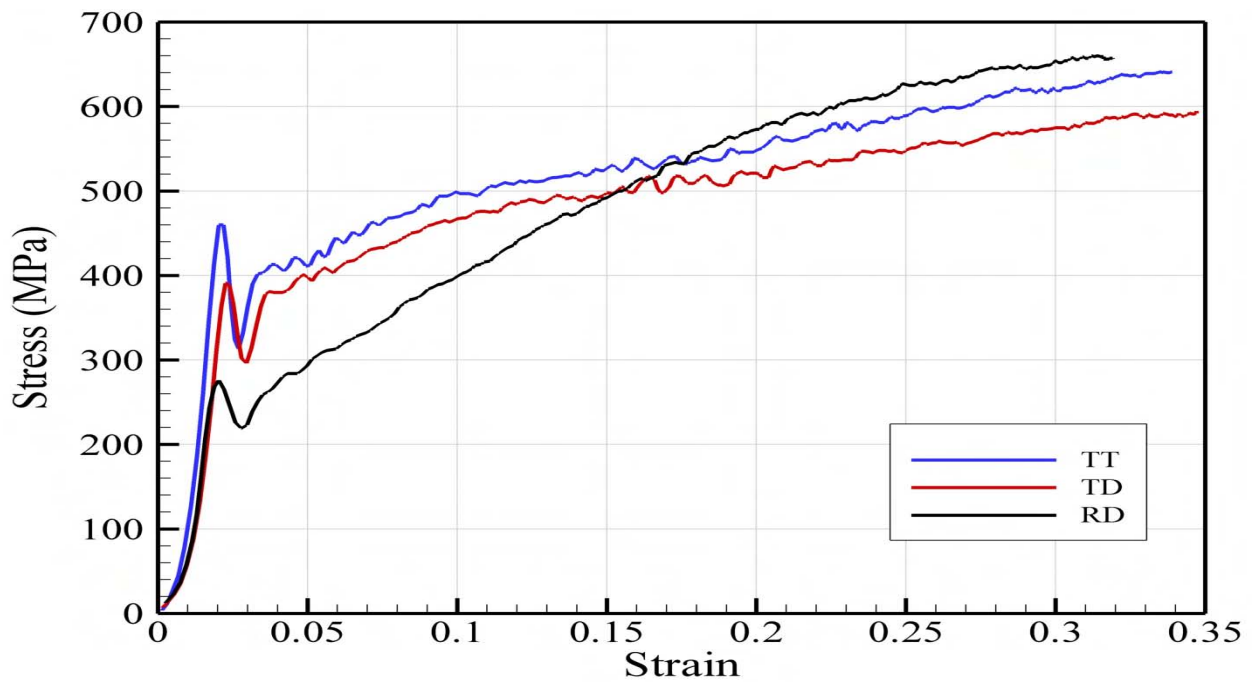


Figure 60: Experimental compression results showing that the high-strain rate response at 400/s is orthotropic.

Table 7: Quasi-static and high rate compressive yield values in the RD, TD, and TT directions, respectively and anisotropy ratios for the material under high-rate loading

Strain	High Rate				Quasi-static			
	RD	TD	TT	Max/Min	RD	TD	TT	Max/Min
0.05	411	398	294	1.398	225	276	330	1.467
0.1	498	467	399	1.248	271	307	361	1.332
0.15	537	498	492	1.091	323	331	389	1.204
0.2	548	521	573	1.099	379	352	419	1.190
0.25	589	548	626	1.142	426	388	448	1.155
0.3	620	575	654	1.137	456	418	477	1.141
0.35	NA	NA	NA	NA	493	452	505	1.117
0.4	NA	NA	NA	NA	522	483	537	1.112

Note also, the strongly non-linear strain hardening behavior of the material in the RD compression, with an abrupt change in the slope of the stress-strain curve at 15% strain, which is indicative of significant twinning. The change in hardening rate is even more dramatic at high rate than at quasi-static loading rate. This is not completely unexpected as it has been observed by [1] that titanium twins more readily as loading rate increases. In general, irrespective of the loading orientation, the yield stress increases with increasing loading rate.

The tests have also revealed that the tension-compression asymmetry in the high-strain rate regime is highly directional. Figure 61 A) shows a comparison between the high -rate results for uniaxial loading in the TD direction in tension and compression, respectively. The initial yield points are very close but as more deformation occurs the strength in compression becomes somewhat larger. This may indicate that some twinning is occurring in the compression loading but this has not been confirmed by post test metallography. Comparisons of high rate compression data with quasi-static data for the TD are shown in Figure 61 B). A clear increase in strength is observed but the hardening rate remains nearly unchanged.

The high rate results for compressive uniaxial loading in the TT direction compared to data gathered at quasi-static loading rates is shown in Figure 62. Again, a clear increase in strength with loading rate is observed with very little change in hardening rate. Due to geometry constraints, no through thickness tension data could be obtained at high rates of loading.

Results at high- rate uniaxial loading in the RD are shown in Figure 63 A). As for loading in TD direction, the initial yield levels are similar but the difference increases with additional strain. This difference increases at a much higher rate than for the TD data. There is also a clear change in hardening, which indicates that significant twinning is occurring. Figure 63 B) shows the comparison with quasi-static data where post test metallography showed a significant amount of twinning. The data indicates that even higher levels of twinning may be occurring at the higher loading rates.

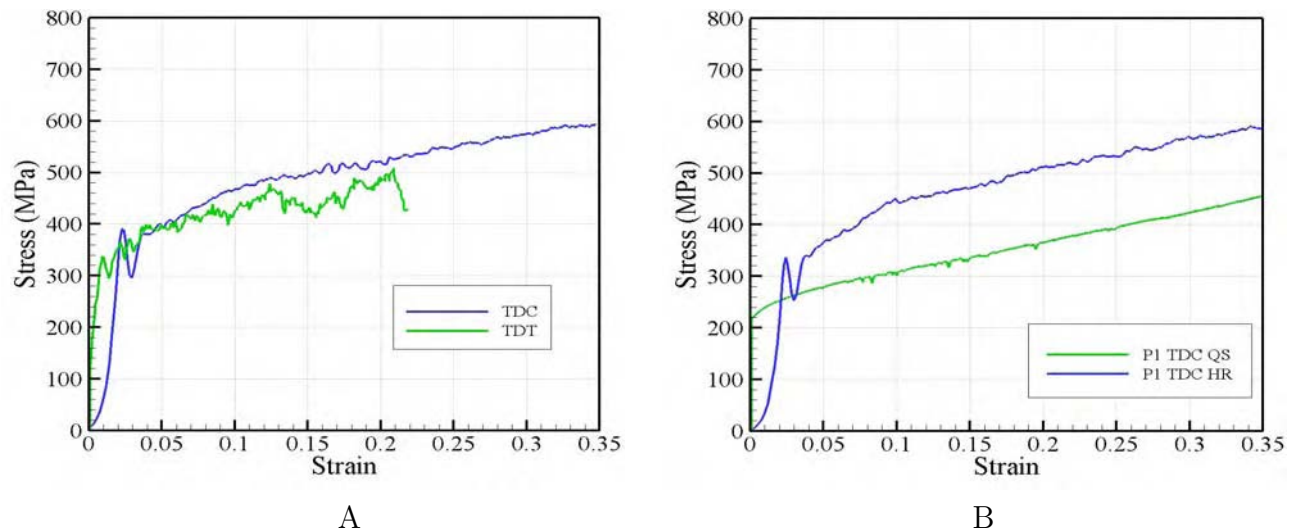


Figure 61: A) Experimental high rate data for uniaxial loading in the TD direction in tension and compression, respectively, and B) Effect of the strain-rate in the response: comparison of experimental high rate data to experimental quasi-static data

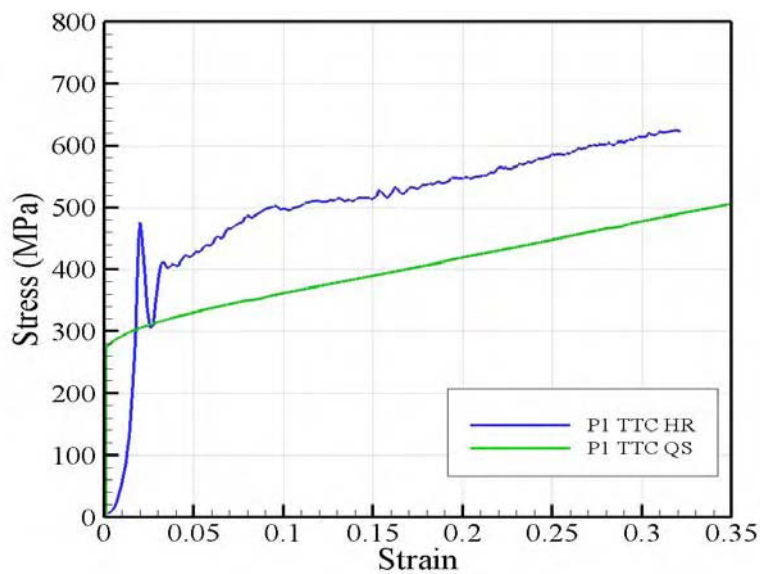


Figure 62: Comparison of compressive high rate to quasi-static data in the TT direction

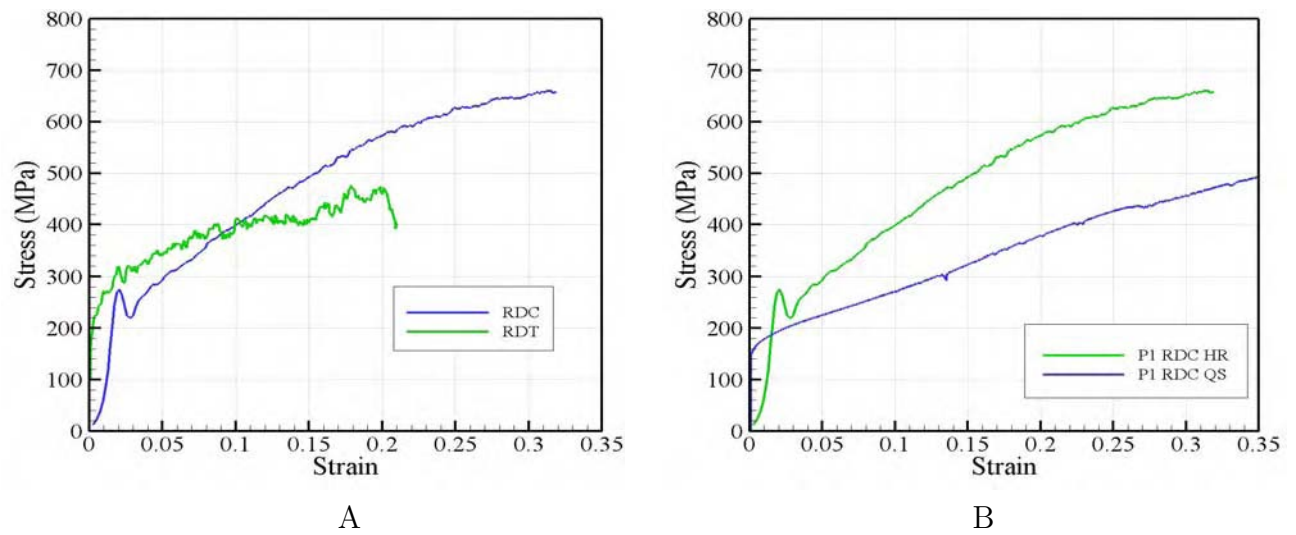


Figure 63: A) Comparison between experimental high rate response in uniaxial loading along the RD direction for tension and compression, respectively; B) Comparison of high rate data to quasi-static data for loading along the RD direction

## 5 Discussion and Conclusions

As already stated, a primary goal of this research was to advance the current state-of-the-art by developing user-friendly, micro-structurally based and numerically robust macroscopic constitutive models that can capture with accuracy the particularities of the plastic response of hexagonal metals, in particular high purity titanium. It has been demonstrated that this goal has been met to a large degree. A comprehensive set of experiments were conducted in order to understand the response of high-purity titanium at room temperature and consequently model the observed response at different strain rates. A series of monotonic quasi-static uniaxial tension and compression tests were conducted to quantify the plastic anisotropy and the tension-compression asymmetry of this material. In addition, four-point bending tests were conducted. To characterize the material's strain rate sensitivity, Split Hopkinson Pressure Bar tests at strain rates of 400 to 600  $\text{sec}^{-1}$  were performed along the axes of symmetry of the material. To gain insight into the deformation mechanisms, OIM and texture evaluations were also conducted in conjunction with the mechanical tests. The experimental activities were complemented with multi-scale model development in the framework of plasticity. The material parameter identification procedure is also outlined. The algorithmic aspects related to the implementation of the models developed in the Finite-Element code EPIC are presented in detail. The ability of the proposed model to capture the main features of the observed behavior is examined by comparing the experimental data with simulation results in terms of stress-strain response in tension/compression and bending for different orientations with respect to the axes of symmetry of the material. Comparison between proposed theory and data are extremely good. This integrated experimental-theoretical effort appears to have resulted in the description, for the first time, of the anisotropic stress-response of high-purity  $\alpha$ -titanium at room temperature. Further research is needed to explore other loading environments but this work has shown that the proposed model can describe with great accuracy the anisotropy induced by texture evolution during monotonic loading. The ability to incorporate data from other loading conditions is already in place. Although, this research was concerned primarily with high purity titanium, it is clear that the proposed model and implementation approach is applicable to other hexagonal materials.

## References

- [1] Gray, G. T., 1997. Influence of strain-rate and temperature on structure/property behavior of high-purity titanium. *Journal de Physique*. IV, 7, 423–428.
- [2] Follansbee, P.S., Gray III, G.T., 1989. An analysis of the low temperature, low and high strain-rate deformation of Ti–6Al–4V. *Metall. Trans. A* 20 A (5), 863–874.
- [3] Lee, W.S., Lin, M.T., 1997. The effects of strain rate and temperature on the compressive deformation behavior of Ti–6Al–4V alloy. *J. Mater. Proc. Tech.* 71, 235–246.
- [4] Nemat-Nasser, S., Guo, Wei-Guo, Nesterenko, Vitali F., Indrakanti, S.S., Gu, Ya-Bei, 2001. Dynamic response of conventional and hot isostatically pressed Ti–6Al–4V alloys: experiments and modeling. *Mech. Mater.* 33 (8), 425–439.
- [5] Picu, R.C., Majorell, A., 2002. Mechanical behavior of Ti–6Al–4V at high and moderate temperatures Part II: constitutive modeling. *Mater. Sci. Eng. A*. 326, 306–316.
- [6] Khan, A.S., Suh, Y.S., Kazmi, R., 2004. Quasi-static and dynamic loading responses and constitutive modeling of titanium alloys. *Int. J. Plast.* 20, 2233–2248.
- [7] Khan, A.S., Kazmi, R., Farroch, B., 2007. Multiaxial and non-proportional loading responses, anisotropy and modeling of Ti–6Al–4V titanium alloy over wide ranges of strain rates and temperatures. *Int. J. Plast.* 23, 931–950.
- [8] Salem, A.A., Kalidindi, S. R., and Doherty, R. D., 2003. Strain hardening of titanium: role of deformation twinning. *Acta Mater.* 51, 4225–4237.
- [9] Li, Q., Xu, Y.B., Bassim, M.N., 2004. Dynamic mechanical behavior of pure titanium. *J. Mater. Proc. Tech.*, 155, 1889–1892.
- [10] Chun, Y. B., Yu, S. L., Semiatin, S. L., and Hwang, S. K., 2005. Effect of deformation twinning on microstructure and texture evolution during cold rolling of CP-titanium. *Mat.Sci. Eng. A* 398, 209–219.
- [11] Lee, D. and Backofen, W. A., 1966. Yielding and plastic deformation in textured shett of titanium and its alloys. *TMS–AIME*, 236, 1966–1703.
- [12] Hill, R., 1948. A theory of the yielding and plastic flow of anisotropic metals. *Proc. Roy. Soc. London A* 193, 281–297.
- [13] Kuwabara, T., Katami, C. Kikuchi, M. Shindo, T. and Ohwue, T., 2001. Cup drawing of pure titanium sheet -finite element analysis and experimental validation., *Proc. 7th Int. Conf. Numerical Methods in Industrial Forming Processes, Toyohashi, JAPAN, 18-20 June 2001*, 781–787.
- [14] Hosford, W., 2005. *Mechanical Behavior of Materials*. Cambridge University Press.

- [15] Staroselsky, A., Anand, L., 2003. A constitutive model for HCP metals deforming by slip and twinning: application to magnesium alloy AZ31B. *Int J. Plast.* 19, 1843–1864.
- [16] Wu, X., Kalidindi, S. R., Necker, C. and Salem, A., 2007. Prediction of crystallographic texture evolution and anisotropic stress-strain curves during large plastic strains in high purity  $\alpha$  titanium using a Taylor-type crystal plasticity model.
- [17] Tome, C. N. and Lebensohn, R. A., 2004. Self-consistent homogenization methods for texture and anisotropy. In: *Continuum Scale Simulation of Engineering Materials*, Ch. 8, D. Raabe, F. Roters, F. Barlat and L.-Q. Chen (Eds.), Wiley-VCH, Weinheim, 473–497.
- [18] Proust, G., Tome, C. N., and Kaschner, G. C., 2007. Modeling texture, twinning, and hardening evolution during deformation of hexagonal materials. *Acta Mater.* 55, 2137–2148.
- [19] Tome, C. N., Maudlin, P. J., Lebensohn, R. A. and Kaschner, G. C., 2001. Mechanical Response of zirconium–I. Derivation of a polycrystal constitutive law and finite element analysis. *Acta Mater.* 49, 3085–3096.
- [20] Cazacu, O., Barlat, F., 2001. Generalization of Drucker’s yield criterion to orthotropy. *Mathematics and Mechanics of Solids*, 6, 613–630.
- [21] Cazacu, O., Barlat, F., 2003. Application of representation theory to describe yielding of anisotropic aluminum alloys. *Int. J. Eng. Sci.* 41, 1367–1385.
- [22] Barlat, F., Cazacu, O., Zyczkowski, M., Banabic, D. and Yoon, J.W., 2004. Yield surface plasticity and anisotropy in sheet metals. In: *Continuum Scale Simulation of Engineering Materials, Fundamentals -Microstructures - Process Applications*, Weinheim, Wiley-VCH Verlag Berlin GmbH, 145–178.
- [23] Barlat, F., Yoon, J.W., Cazacu, O., 2007. On linear transformation-based anisotropic yield functions. *Int J. Plast.* , 23, 876–896.
- [24] Cazacu, O., Barlat, F., 2004. A criterion for description of anisotropy and yield differential effects in pressure-insensitive metals. *Int. J. Plast.*, 20, 2027–2045.
- [25] Hosford, W.F., Allen, T.J., 1973. Twinning and directional slip as a cause for strength differential effect. *Met. Trans.* 4, 1424–1425.
- [26] Vitek, V, Mrovec, M., Bassani, J.L., 2004. Influence of non-glide stresses on plastic flow: from atomistic to continuum modeling. *Mater. Sci Eng. A.* vol. 365, 31–37.
- [27] Cazacu, O. and Barlat, F., 2008. Modeling plastic anisotropy and strength differential effects in metallic materials. In: *Multiscale modeling of heterogeneous materials: from microstructure to macro-scale properties*, ISTE Ltd and John Wiley Inc., 71–87.
- [28] Graff, S., Brocks, W. and Dirk Steglich, 2007. Yielding of magnesium: From single crystal to polycrystalline aggregates *Int J. Plast.*, 23., 1957-1978

- [29] Cazacu, O., Plunkett, B., Barlat, F., 2006. Orthotropic yield criterion for hexagonal closed packed metals. *Int. J. Plast.* 22, 1171–1194.
- [30] Kelley, E.W., Hosford, W.F., 1968. Deformation characteristics of textured magnesium. *Trans. TMS-AIME* 242, 654–661.
- [31] Plunkett, B., Cazacu, O., Lebensohn, R. A. and Barlat, F., 2006. Evolving yield function of hexagonal materials taking into account texture development and anisotropic hardening. *Acta Mater.*, 54, 4159–4169.
- [32] Lebensohn, R.A., and Tome, C.N., 1993. A self-consistent anisotropic approach for the simulation of plastic deformation and texture development of polycrystals: Application to zirconium alloys. *Acta Metall. Mater.* 41, 2611–2624.
- [33] Plunkett, B., Cazacu, O., Lebensohn, R. A. and Barlat, F., 2007. Elastic-viscoplastic anisotropic modeling of textured metals and validation using Taylor cylinder impact test. *Int. J. Plast.* 23, 1001–1021.
- [34] Cazacu, O. and Barlat, F., 2008. Viscoplastic modeling of anisotropic textured metals. In: *Multiscale modeling of heterogeneous materials: from microstructure to macro-scale properties*, ISTE Ltd and John Wiley Inc., 111–126.
- [35] Lou, X., Li, M., Boger, R., Agnew, S., Wagoner, R., 2006. Hardening evolution of AZ31B Mg sheet. *Int. J. Plast.* 23, 44–86.
- [36] Salem, A.A., Kalidindi, S. R., and Lemiatin, S. L., 2005. Strain hardening due to deformation twinning in  $\alpha$  titanium: Constitutive relations and crystal-plasticity modeling. *Acta Mater.* 53, 3495–3502.
- [37] Hung, P.C., Voloshin, A. S., 2003. In-plane strain measurement by digital image correlation. *J. of the Braz. Soc. of Mech. Sci. and Eng.*, XXXV(3), 215–221.
- [38] Miguil-Touchal, Morestin, S., Brunet, M., 1997. Various applications of digital image correlation method. In: Brebbia, C. A., Anagnostopoulos, P., Omagno, G.C. (Eds) *Computational methos in experimental measurements VIII. Vol. Modeling and Simulation*, 17, Trans. Wessex Institute.
- [39] Chichili, D.R., Ramesh, K.T., Hemker, K.J., 2004. Adiabatic shear localization in  $\alpha$ -titanium. *J. Mech. Phys. Solids* 52, 1889–1909.
- [40] Dawson, P. R., Macewen, S. R. and Wu, P.D., 2003. Advances in sheet metal forming analyses: dealing with mechanical anisotropy from crystallographic texture, *Int. Materials Reviews*, 48, 86–115.
- [41] *Materials Handbook 15th Edition* Mc.Graw-Hill Handbooks, Eds. Bradley, G.S., Clauser, H. R. and Vaccari, H. R.

- [42] Hung, P.C., Voloshin, A. S., 2003. In-plane strain measurement by digital image correlation. *J. of the Braz. Soc. of Mech. Sci. and Eng.*, XXXV(3), 215–221.
- [43] Miguil-Touchal, Morestin, S., Brunet, M., 1997. Various applications of digital image correlation method. In: Brebbia, C. A., Anagnostopoulos, P., Omagno, G.C. (Eds) *Computational methos in experimental measurements VIII*. Vol. Modeling and Simulation, 17, Trans. Wessex Institute.
- [44] Song SG, Gray III GT. Structural interpretation of the nucleation and growth of deformation twins in Zr and Ti- II. TEM study of twin morphology and defect reactions during twinning, 1995. *Acta Metal.* 43, 2339–2350.
- [45] Pironneau, O. (1989), *Finite element methods for fluids*, John Wiley & Sons Ltd., Chichester.
- [46] Anand, L. and Kothari, M. (1996) A computational procedure for rate-independent crystal plasticity. *J. Mech. Phys. Solids* , 44, 525–558.
- [47] Asaro, R.J. and Rice, J. R. (1977) Strain localization in ductile single crystals. *J. Mech. Phys. Solids* , 25, 309–338.
- [48] Asaro, R.J. and Needleman, A. (1985) Texture development and strain hardening in rate dependent polycrystals. *Acta. Metall.* , 33, 923–953.
- [49] Bishop, J.F.W. and Hill, R. (1951a) A theory of plastic distortion of a polycrystalline aggregate under combined stresses. *Phil. Mag.*, 42, 414–427.
- [50] Bishop, J.F.W. and Hill, R. (1951b) A theoretical derivation of the plastic properties of a polycrystalline face-centered metal. *Phil. Mag.*, 42, 1298–1307.
- [51] Busso, E. P. and Cailletaud, G. (2005) On the selection of active slip systems in crystal plasticity. *Int. J. Plasticity*, 12, 1–28.
- [52] O. Cazacu and I.R. Ionescu (2006), Compressible rigid visco-plastic fluids, *J. of Mech. Phys. of Solids*, Vol. 54, issue 8, 1640–1667.
- [53] Chang, Y.W. and Asaro, R. J. (1981) An experimental study of shear localization in aluminum-copper single crystals. *Acta. Metall.*, 29, 241–250.
- [54] Crone, W.C., Shield, T.W., Creuziger, A., Henneman B. (2004). Orientation dependence of the plastic slip near notches in ductile FCC single crystals, *J. Mech. Phys. Solids* , 52, 85–112.
- [55] Delannay, L., Jacques, P. J. and Kalidindi, S. R. (2006) Finite element modeling of crystal plasticity with grains shaped as truncated octahedrons. *Int. Journal of Plast.*, 22,
- [56] Fortin, M. and Glowinski, R. (1982), *Methodes de Lagrangien augmentés, application à la résolution de problèmes aux limites*, Dunod.

- [57] Franciosi, P. (1985) The concepts of latent hardening and strain hardening in metallic single crystals. *Acta Metall*, 33, 1601–1612.
- [58] Gan, Y. X., Kysar, J. W. and Morse, T. L. (2006), Cylindrical void in a rigid-ideally plastic single crystal II: Experiments and simulations, *Int. J. of Plasticity*, 22 39–72.
- [59] Glowinski, R. and Le Tallec, P. (1989), *Augmented Lagrangian and Operator Splitting method in Non-Linear Mechanics*, SIAM Studies in Applied Mathematics.
- [60] Hill, R and Havner, K.S. (1982) Perspectives in the mechanics of elastoplastic crystals. *J. Mech. Phys. Solids* , 30, 5–22.
- [61] Hill, R. (1966) Generalised constitutive relations for incremental deformation of metal crystals for multislip. *J. Mech. Phys. Solids*, 14, 95 –102.
- [62] Hill, R and Rice, J.R. (1972) Constitutive analysis of elastic-plastic crystals at arbitrary strain. *J. Mech. Phys. Solids* , 20, 401–413.
- [63] Hutchinson, J. W. (1976) Bounds and selfconsistent estimates for creep of polycrystalline materials. *Proc. R. Soc. Lond. A* , 348, 101–127.
- [64] (1993) A self-consistent anisotropic approach for the simulation of plastic deformation and texture development of polycrystals: Application to zirconium alloys. *Acta Metall. Mater.*, 41, 2611–2624.
- [65] Kok, S., Beaudoin, A. J., and Tortorelli, D. A. (2002) A polycrystal plasticity model based on the mechanical threshold. *Int. Journal of Plast.*, 18, 715–741.
- [66] Kuchnicki, S. N. (2008) An explicit formulation for multiscale modeling of bcc metals. *Int. Journal of Plast.*, in press.
- [67] Mandel, J. (1965) Generalisation de la plasticite de W.T. Koiter. *Int. J. Eng. Solids Struct*, 1, 273–295.
- [68] McGinty, R. and McDowell, D. (2006) A semi-implicit integration scheme for rate independent finite crystal plasticity. *Int. Journal of Plast.*, 22, 996–1025.
- [69] Peirce, D. Asaro, R.J. and Needleman, A. (1982) An analysis of nonuniform and localized deformation in ductile single crystals. *Acta Metall.* 30, 1087–1119.
- [70] Peirce, D. Asaro, R.J. and Needleman, A. (1983) Material rate dependence and localized deformation in crystalline solids. *Acta Metall.* 31, 1951–1976.
- [71] Pironneau, O. (1989), *Finite element methods for fluids*, John Wiley & Sons Ltd., Chichester.
- [72] Rice, J.R. (1971) Inelastic constitutive relations for solids: an internal variable theory and its application to metal plasticity. *J. Mech. Phys. Solids* , 19, 433–455.

- [73] Rice, J.R. (1987) Tensile crack tip fields in elastic-ideally plastic crystals. *Mech. of Materials*, 6, 317–335.
- [74] Schmidt-Baldassari, M., (2003) Numerical concepts for rate-independent single crystal plasticity. *Comp.Methods Appl. Mech. Engng.* 192, 1261–1280.
- [75] Taylor, G.I. and Elam, C. F. (1923) The distortion of an aluminum crystal during a tensile test. *Proc. Royal Soc. London A* 102, 643–647.
- [76] Taylor, G.I. (1934) The distortion of an aluminum crystal during a tensile test. *Proc. Royal Soc. London A* , 643–647.
- [77] Taylor, G.I. and Elam, C. F. (1925) The plastic extension and fracture of aluminum single crystals.*Proc. Royal Soc. London A* 108, 28–51.
- [78] Taylor, G.I. (1938) Plastic strains in metals. *J. Institute of Metals* 62, 307–324.
- [79] Taylor, G.I. (1938) Analysis of plastic strain in a cubic crystal. *Stephen Timoshenko 60th Anniversary Volume*, 218–224, McMillan Co., New York.
- [80] Teodosiu, C. (1975)A physical theory of the finite elastic-viscoplastic behavior of single crystals. *Eng. Trans.*, 23, 151–170.
- [81] Teodosiu, C. and Sidoroff, F (1976) A theory of finite elastoviscoplasticity of single crystals *Int J Engng. Sci.*, 14, pp. 165–176.
- [82] Temam, R.(1979),*Navier-Stokes Equations. Theory and Numerical Analysis*, North-Holland, Amsterdam.
- [83] Van Houtte, P., Li, S. and Engler,O. (2004) Taylor type homogenization methods for texture and anisotropy. in *Continuum scale simulations of engineering materials*, Eds. D. Raabe, F. Roters, F. Barlat, L-Q Chen, Wiley-VCH.